

Generalized Linear Response Theory for Pumped Systems and its Application to Transient Optical Properties within DPOA

Amir Eskandari-asl¹ and Adolfo Avella^{1,2,3}

¹*Dipartimento di Fisica “E.R. Caianiello”, Università degli Studi di Salerno, I-84084 Fisciano (SA), Italy*

²*CNR-SPIN, Unità di Salerno, I-84084 Fisciano (SA), Italy and*

³*CNISM, Unità di Salerno, Università degli Studi di Salerno, I-84084 Fisciano (SA), Italy*

We derive the two-time linear response theory for out-of-equilibrium pumped systems, generic pump-probe delays and probe frequencies. Such a theory enormously simplifies the numerical calculations, for instance, of the optical conductivity with respect to the actual procedure, which requires computing the effect of the probe pulse for each time delay with respect to the pump pulse. The theory is given for a generic observable and pumped Hamiltonian and then specialized for a system with a quadratic Hamiltonian and its transient optical properties, exploiting the Dynamical Projective Operatorial Approach (DPOA). The theory is complemented by a set of crucial numerical guidelines that help perform actual calculations in a computationally affordable way. The optical response (differential transient reflectivity and absorption) of a prototypical three-band (core, valence, and conduction) model in the XUV regime is analyzed in detail to illustrate the theory and its application. Using some generalizations of the density of states, we provide a systematic approach to exploring the optical properties in terms of the system band structure features and the pump parameters. Such an analysis can be extremely helpful in understanding the actual results of experimental optical measurements. Moreover, we study the effects of inter-band and intra-band transitions, the local dipole coupling, and single and multi-photon processes. The latter is further investigated by varying the central frequency of the pump pulse to have different regions of the first Brillouin zone in resonance with it. We also study the effect of varying the pump pulse intensity. Finally, we study and analyze the transient optical properties in the probe pulse regime of IR and visible.

I. INTRODUCTION

Thanks to modern technological developments, studying the real-time dynamics of condensed matter systems in the ultra-fast attosecond regime is now possible. For such studies, one deals with the so-called pump-probe setups, where a system is driven out-of-equilibrium by an intense ultra-short electromagnetic pump pulse and is investigated using a rather low-intensity probe pulse, as a function of the time delay between the two pulses [1–5]. The study of the real-time dynamics of ultra-fast electronic excitation in the attosecond regime unravels the fundamental physical transitions in the pumped system [6–10]. This knowledge is relevant for fundamental physics and future ultra-fast electro-optical circuit and device engineering.

Several different approaches can experimentally investigate the pumped systems. One way is to study the high harmonic generation (HHG), where one studies the radiations generated by the pumped system with frequencies of integer multiples of the pump frequency [11–20]. Another approach to studying the pumped system is the time-resolved angle-resolved photoemission spectroscopy (TR-ARPES) [10, 21–28], where analyzing the energy and momentum distribution of the electrons ejected from the pumped system via photoelectric effect as a function of the time delay between the pump and probe pulses, one determines the out-of-equilibrium electronic properties. Another way for studying the pumped systems is through measuring the transient dynamical variations of their optical responses to a weak probe pulse [6, 17, 29–

38]. In this work, we focus on the latter and provide a convenient theoretical tool to facilitate this analysis.

For studying the transient optical properties, one usually studies the dynamical variation of the absorption coefficient [6, 17, 29, 31–35, 37] or the reflectivity [29, 30, 36, 38, 39] of the probe pulse as a function of the probe-pulse frequency (or equivalently, probe photon energy) and the time delay between the pump and probe pulses. Varying the photon energy of the probe pulse, one can study different energy ranges of the band structure and their corresponding dynamical excitation transitions. A very convenient optical approach to reveal the pumping mechanisms in solids is to use a probe pulse with a much higher frequency than the pump pulse. In such a scenario, an intense low-frequency (e.g., in the IR or visible ranges) laser pulse pumps the system out of equilibrium by altering the electronic bands and distributions for the energies near the Fermi level. At the same time, the strongly bounded *core* electrons are left almost unaltered. The high-frequency (e.g., in the XUV range) probe pulse then scans those out-of-equilibrium electronic levels by exciting the *core* electrons to them [6, 17, 29, 31–38]. The recent experimental setups exploit pump pulses with durations of the order of tens of femtoseconds and probe them with even shorter delay times [17, 29, 31–33, 35, 37, 38]. Such ultra-short time intervals rule out several relaxation transitions on longer time scales, including instantaneous emission, electron-phonon interaction, etc. This is of fundamental interest as one can study pure early-time electronic dynamics with several potential technological applications, such as

manufacturing high-speed electronics.

On the theory side, the standard approach to numerically simulate the pumped systems is the time-dependent density functional theory (TD-DFT) [35, 38, 40–47], which is capable of considering different kinds of interactions up to some approximations. However, there are two relevant drawbacks in TD-DFT: (i) the computational cost is very high, and (ii) it's more complex to get deep insight into the underlying physics of the results of the simulations. On the other hand, the model-Hamiltonian approaches, which generally allow a better understanding of the underlying physical phenomena, usually suffer from the problem of oversimplification [35, 48].

To overcome some of the limitations and drawbacks of the current theoretical approaches, we have developed a method, dubbed the Dynamical Projective Operatorial Approach (DPOA), and applied it to a pumped germanium sample [38]. We benchmarked our results with those of TD-DFT on a rough momentum grid (to be affordable for TD-DFT). Then, we extended our study to much finer momentum grid, showing that the latter was necessary to truly understand the complicated transitions in the actual material and clarify the individual roles of different mechanisms and their interplay effects. Moreover, being capable of computing all multi-time multi-particle correlation functions using DPOA, we extended the theory to study TR-ARPES. We showed how one can study the effects and interplays of different pumping mechanisms, as well as the role of crystal symmetry in the TR-ARPES signal, and how various types of sidebands emerge [49].

Theoretical study and numerical simulation for the optical properties is much heavier than the other scenarios (HHG and TR-ARPES), as for each value of the time delay between the pump and probe pulses, one needs to compute the current in the presence of both pulses and then subtract the current induced by the pump pulse only from it, to obtain the two-time optical conductivity that can be Fourier transformed to get the out-of-equilibrium dielectric function and, finally, the transient reflectivity and absorption. Given that in the experimental setups, they consider very many time delays, performing TD-DFT simulations becomes extremely heavy and challenging, and one usually needs to use a sparse sampling of the first Brillouin zone (FBZ) by exploiting a rough momentum grid, which may indeed result in losing some relevant features in the simulations.

Instead, one can get a noticeable simplification by exploiting an out-of-equilibrium version of the linear response theory (LRT), where the two-time linear response of the pumped system to the probe pulse is computed. This latter is the core of this work, where the out-of-equilibrium LRT formulation is given for a general case. Then, it is specialized for a pumped lattice system with an effective quadratic Hamiltonian within DPOA. After that, we apply the out-of-equilibrium LRT to obtain the optical conductivity and, consequently, the dielectric function, from which one, in principle, can calcu-

late the reflectivity and absorption coefficient. We apply this theory to a prototypical three-band model and study the different out-of-equilibrium optical behaviors that can emerge in various regimes.

The rest of this article is organized as follow. In Sec. II, we report the derivation of the two-time linear response theory for an out-of-equilibrium pumped system (Sec. II A), its specialization to lattice systems with quadratic Hamiltonians (Sec. II B), and to their optical conductivity (Sec. II C), reflectivity and absorption (Sec. II D), and delve into the equilibrium case too (Sec. II E). We also report some important guidelines for numerical calculations (Sec. II F): a simplified and numerically effective rewriting of the optical conductivity expression (Sec. II F 1), a discussion on how to choose the value of the unavoidable damping factor (Sec. II F 2), a possible analytical simplification, leading to a significant reduction of the calculation time, regarding the time range after the application of the pump pulse (Sec. II F 3), two possible approximations regarding the core levels (Sec. II F 4) and a quasi-static dynamics (Sec. II F 5). In Sec. III, we define (Sec. III A) and study a prototypical three-band (core, valence, and conduction) model in presence of only the Peierls substitution coupling (Sec. III B) and analyze the effects of inter- and intra-band transitions driven by the pump pulse in the model (Sec. III C). After that, we consider both the Peierls substitution and the dipole couplings (Sec. III D) to study the features originating from the latter. Then, going back to the case of having only the Peierls substitution coupling, we study the dependence of the observed features on the frequency (Sec. III E) and the intensity (Sec. III F) of the pump pulse. Moreover, we investigate the optical properties in the probe pulse ranges of the infrared (IR) and visible (Sec. III G). Sec. IV summarizes this work. Finally, we have a plethora of appendices discussing: the linear variation of the density matrix in the presence of the probe pulse (Sec. A), the dielectric function and the reflectivity formula out of equilibrium (Sec. B), the approximation related to considering only the transitions from the core levels in optical conductivity (Sec. C), the cancellation of the equilibrium low-frequency (static) tails at zero temperature (Sec. D), the quasi-static approximation (Sec. E), the damping factor 0^+ (Sec. F), the transient differential dielectric function (Sec. G), the density of states and its generalizations (Sec. H), and the intra-band motion with different pump-pulse frequencies (Sec. I).

II. THEORY

A. Linear response in pump-probe setups

In a pump-probe experimental setup, the sample is pumped using an intense electromagnetic pulse (e.g., an IR pulse) and probed by another pulse (e.g., an ultra-short XUV pulse) of much lower intensity (usually just

above the signal-to-noise ratio threshold). Accordingly, the response of the system to the pump pulse is usually highly non-linear and very complex, and requires a full-fledged quantum-mechanical theoretical description even when the electromagnetic field is described just classically through its time-dependent vector and scalar potentials. On the other hand, the response of the pumped system to the probe pulse can be safely studied up to the first order in the probe pulse, that is within the linear response theory. This can be exploited to greatly simplify theoretical description of pump-probe setups. In the following, we derive and describe a comprehensive theoretical formulation to compute the linear response of a pumped system to a probe pulse.

The Hamiltonian that describes a system in a pump-probe setup, $\hat{H}(t)$, can be written as

$$\hat{H}(t) = \hat{H}'(t) + \hat{H}''(t), \quad (1)$$

where $\hat{H}'(t)$ is the Hamiltonian describing the pumped system and $\hat{H}''(t)$ is the Hamiltonian describing the interaction between the system and the probe pulse (the probe Hamiltonian), with respect to which we will compute the linear response. $\hat{H}'(t)$ is given by the sum of the Hamiltonian describing the system at equilibrium, \hat{H}_0 , and the Hamiltonian describing the coupling between the system and the pump pulse, $\hat{H}_{\text{pu}}(t)$ (the pump Hamiltonian),

$$\hat{H}'(t) = \hat{H}_0 + \hat{H}_{\text{pu}}(t). \quad (2)$$

We assume that, at an initial time t_{ini} (e.g., $t_{\text{ini}} \rightarrow -\infty$), both pump and probe Hamiltonians vanish and the system is at equilibrium.

Given an observable that describes a type of response of the system to the pump and probe pulses (e.g., the charge, spin, or orbital current density, the polarization density, the magnetization density, etc.) and the corresponding operator in the Schrödinger picture, $\hat{O}(t)$, which can generally be time dependent, its linear response to the probe pulse has two components. The first component arises from the evolution in time of the state of the system under the application of the pump and probe pulses and can be fully taken into account through the corresponding evolution in time of the density matrix of the system. The second component is present if there is a dependence of the operator $\hat{O}(t)$ on the probe pulse applied to the system.

To obtain the first component, we define an interaction picture where $\hat{H}'(t)$ acts as the *non-interacting* Hamiltonian (with respect to the probe pulse; coupling to the pump pulse is fully taken into account) and $\hat{H}''(t)$ acts as the *interaction* Hamiltonian. Any operator $\hat{Q}(t)$ in the Schrödinger picture transforms to such interaction picture via

$$\hat{Q}_{H'}(t) = \hat{U}'(t_{\text{ini}}, t) \hat{Q}(t) \hat{U}'(t, t_{\text{ini}}), \quad (3)$$

where $\hat{U}'(t_1, t_2)$ is the time propagator given in Eq. A3 of the App. A.

As it is reported in the App. A, it is straightforward to show that the linear variation (with respect to probe Hamiltonian) of the many-body density matrix of the system $\hat{Y}(t)$ (both pump and probe pulses applied) upon the application of the probe pulse is given by

$$\hat{Y}(t) - \hat{Y}'(t) = -\frac{i}{\hbar} \int_{t_{\text{ini}}}^t dt' \hat{U}'(t, t_{\text{ini}}) \left[\hat{H}''_{H'}(t'), \hat{Y}_0 \right] \hat{U}'(t_{\text{ini}}, t), \quad (4)$$

where $\hat{Y}'(t) = \hat{U}'(t, t_{\text{ini}}) \hat{Y}_0 \hat{U}'(t_{\text{ini}}, t)$ is the many-body density matrix of the system with no probe pulse applied and $\hat{Y}_0 = \hat{Y}(t_{\text{ini}})$ is the equilibrium many-body density matrix of the system (nor pump neither probe pulse applied).

The first component of the linear response, $\delta_1 \langle \hat{O}(t) \rangle_t$, comes from the variation of the density matrix and can be written as

$$\delta_1 \langle \hat{O}(t) \rangle_t = \text{Tr} \left(\hat{O}(t) \left[\hat{Y}(t) - \hat{Y}'(t) \right] \right), \quad (5)$$

and, up to the linear order in the probe Hamiltonian, is given by

$$\delta_1 \langle \hat{O}(t) \rangle_t = -\frac{i}{\hbar} \int_{t_{\text{ini}}}^t dt' \left\langle \left[\hat{O}_{H'}(t), \hat{H}''_{H'}(t') \right] \right\rangle_{t_{\text{ini}}}, \quad (6)$$

where we used Eq. 4 and $\langle \dots \rangle_{t_{\text{ini}}} = \text{Tr}(\dots \hat{Y}_0)$ is the expectation value with respect to equilibrium many-body density matrix of the system. Eq. 6 is formally very similar to the Kubo formula at equilibrium.

The second component of the linear response comes from the variation of the operator $\hat{O}(t)$ induced by the application of the probe pulse, and is given by

$$\delta_2 \langle \hat{O}(t) \rangle_t = \left\langle \delta \hat{O}_{H'}(t) \right\rangle_{t_{\text{ini}}}, \quad (7)$$

where $\delta \hat{O}_{H'}(t)$ is the variation of the operator $\hat{O}_{H'}(t)$ up to the linear order in the probe pulse. The total linear response to the probe pulse is then the sum of the two components:

$$\delta \langle \hat{O}(t) \rangle_t = \delta_1 \langle \hat{O}(t) \rangle_t + \delta_2 \langle \hat{O}(t) \rangle_t. \quad (8)$$

B. Pumped lattice systems with quadratic Hamiltonians

In this section, we consider a lattice system with an effective quadratic Hamiltonian $\hat{H}'(t)$,

$$\hat{H}'(t) = \sum_{\mathbf{k}, n_1, n_2} \hat{c}_{\mathbf{k}, n_1}^\dagger h'_{\mathbf{k}, n_1, n_2}(t) \hat{c}_{\mathbf{k}, n_2}, \quad (9)$$

where \mathbf{k} is the crystal momentum that is summed over the first Brillouin zone (FBZ), n_m stands for all other relevant quantum numbers (e.g., band/orbital, spin, etc.), $\hat{c}_{\mathbf{k},n_m}$ ($\hat{c}_{\mathbf{k},n_m}^\dagger$) is the annihilation (creation) operator of an electron in the state with quantum numbers (\mathbf{k}, n_m) , and $h'_{\mathbf{k},n_1,n_2}(t)$ is the matrix element, between the two states (\mathbf{k}, n_1) and (\mathbf{k}, n_2) , of the first-quantization (single-particle) Hamiltonian describing the sample and its coupling to the pump pulse.

We already clarified in the previous section, given the relative low intensity of the probe pulse inherent to its *probing* nature, that one can use the linear response theory to compute the response of the pumped system to the probe pulse. This allows us to safely retain only the lowest order terms in the probe pulse in the probe Hamiltonian, $\hat{H}''(t)$. According to this, in the dipole gauge, $\hat{H}''(t)$ has the following general form

$$\hat{H}''(t) = \sum_{\mathbf{k},n_1,n_2} \hat{c}_{\mathbf{k},n_1}^\dagger \left[\frac{e}{\hbar} \mathbf{V}_{\mathbf{k},n_1,n_2}(t) \cdot \mathbf{A}_{\text{pr}}(t) + e \mathbf{D}_{\mathbf{k},n_1,n_2}(t) \cdot \mathbf{E}_{\text{pr}}(t) \right] \hat{c}_{\mathbf{k},n_2}, \quad (10)$$

where \cdot is the inner product of vectors, $\mathbf{A}_{\text{pr}}(t)$ and $\mathbf{E}_{\text{pr}}(t) = -\partial_t \mathbf{A}_{\text{pr}}(t)$ are the probe-pulse vector potential and electric field, respectively, $-e$ is the charge of electron, and the time- and momentum-dependent vectorial matrix elements $\mathbf{V}_{\mathbf{k},n_1,n_2}(t)$ and $\mathbf{D}_{\mathbf{k},n_1,n_2}(t)$ determine how the vector potential and electric field couple to the sample, respectively. Later, we will give their explicit expressions. We have assumed that the wavelength of the probe pulse is not shorter than the XUV one, which is hundreds of times larger than any lattice constant in *real* materials, so that one can consider the electromagnetic field practically as uniform.

Then, for a generic observable $\hat{O}(t) = \sum_{\mathbf{k},n_1,n_2} \hat{c}_{\mathbf{k},n_1}^\dagger O_{\mathbf{k},n_1,n_2}(t) \hat{c}_{\mathbf{k},n_2}$, the first component of the linear response to the probe pulse is obtained from Eq. 6 as

$$\delta_1 \langle \hat{O}(t) \rangle_t = -\frac{i}{\hbar} \sum_{n_1,n_2,n_3,n_4} \sum_{\mathbf{k}} O_{\mathbf{k},n_1,n_2}(t) \int_{t_{\text{ini}}}^t dt' \left(\frac{e}{\hbar} \mathbf{V}_{\mathbf{k},n_3,n_4}(t') \cdot \mathbf{A}_{\text{pr}}(t') + e \mathbf{D}_{\mathbf{k},n_3,n_4}(t') \cdot \mathbf{E}_{\text{pr}}(t') \right) \left\langle \left[\hat{c}_{H',\mathbf{k},n_1}^\dagger(t) \hat{c}_{H',\mathbf{k},n_2}(t), \hat{c}_{H',\mathbf{k},n_3}^\dagger(t') \hat{c}_{H',\mathbf{k},n_4}(t') \right] \right\rangle_{t_{\text{ini}}}. \quad (11)$$

As a mathematical simplification, without any loss of generality, we consider the electric field of the probe pulse to be a Dirac delta function applied at the time t_{pr} , the probe time,

$$\mathbf{E}_{\text{pr}}(t) = \mathbf{E}_{\text{pr}} \delta(t - t_{\text{pr}}), \quad (12)$$

and, consequently, we have

$$\mathbf{A}_{\text{pr}}(t) = -\mathbf{E}_{\text{pr}} \theta(t - t_{\text{pr}}). \quad (13)$$

Hereafter, we assume that $t_{\text{pr}} \geq t_{\text{ini}}$.

The first component of the linear response to such a probe reads as

$$\delta_1 \langle \hat{O}(t) \rangle_t = -\frac{i}{\hbar} \sum_{n_1,n_2,n_3,n_4} \sum_{\mathbf{k}} O_{\mathbf{k},n_1,n_2}(t) \int_{t_{\text{ini}}}^t dt' \left(-\frac{e}{\hbar} \mathbf{V}_{\mathbf{k},n_3,n_4}(t') \theta(t' - t_{\text{pr}}) + e \mathbf{D}_{\mathbf{k},n_3,n_4}(t_{\text{pr}}) \delta(t' - t_{\text{pr}}) \right) \cdot \mathbf{E}_{\text{pr}} \left\langle \left[\hat{c}_{H',\mathbf{k},n_1}^\dagger(t) \hat{c}_{H',\mathbf{k},n_2}(t), \hat{c}_{H',\mathbf{k},n_3}^\dagger(t') \hat{c}_{H',\mathbf{k},n_4}(t') \right] \right\rangle_{t_{\text{ini}}}. \quad (14)$$

The retarded response function of the system, $\chi(t, t')$, is defined through

$$\delta \langle \hat{O}(t) \rangle_t = \int_{t_{\text{ini}}}^{\infty} dt' \chi(t, t') \cdot \mathbf{E}_{\text{pr}}(t'). \quad (15)$$

Obviously, if \hat{O} is a vector (scalar), χ is a rank 2 (rank 1) tensor. Since the linear response has two components (see Eq. 8), the response function too can be written as the sum of two components, $\chi(t, t') = \chi_1(t, t') + \chi_2(t, t')$, where $\chi_{1(2)}(t, t')$ corresponds to the first (second) component of the linear response to the probe pulse. Given the expression chosen for the probe pulse (Eq. 12), Eq. 15 simplifies to

$$\delta_{1,2} \langle \hat{O}(t) \rangle_t = \chi_{1,2}(t, t_{\text{pr}}) \cdot \mathbf{E}_{\text{pr}}. \quad (16)$$

Comparing Eq. 16 with Eq. 14 and considering the arbitrariness of \mathbf{E}_{pr} , we get the following expression for the first component of the response function

$$\chi_1(t, t_{\text{pr}}) = -\frac{i}{\hbar} \theta(t - t_{\text{pr}}) \sum_{n_1,n_2,n_3,n_4} \sum_{\mathbf{k}} O_{\mathbf{k},n_1,n_2}(t) \int_{t_{\text{ini}}}^t dt' \left(-\frac{e}{\hbar} \mathbf{V}_{\mathbf{k},n_3,n_4}(t') \theta(t' - t_{\text{pr}}) + e \mathbf{D}_{\mathbf{k},n_3,n_4}(t_{\text{pr}}) \delta(t' - t_{\text{pr}}) \right) \left\langle \left[\hat{c}_{H',\mathbf{k},n_1}^\dagger(t) \hat{c}_{H',\mathbf{k},n_2}(t), \hat{c}_{H',\mathbf{k},n_3}^\dagger(t') \hat{c}_{H',\mathbf{k},n_4}(t') \right] \right\rangle_{t_{\text{ini}}}. \quad (17)$$

For the second component of the response function, we need the variation of the operator $\hat{O}(t)$ induced by the application of the probe pulse up to the linear order. We assume that $\hat{O}(t)$ depends on the applied pulses only through their vector potentials. Then, considering the expression chosen for the probe pulse, Eq. 12, we can

write

$$\begin{aligned} \delta_2 \langle \hat{O}(t) \rangle_t &= \sum_{n_1, n_2} \sum_{\mathbf{k}} \frac{\delta O_{\mathbf{k}, n_1, n_2}(t)}{\delta \mathbf{A}(t)} \cdot \mathbf{A}_{\text{pr}}(t) \\ &\quad \left\langle \hat{c}_{H', \mathbf{k}, n_1}^\dagger(t) \hat{c}_{H', \mathbf{k}, n_2}(t) \right\rangle_{t_{\text{ini}}} \\ &= -\theta(t - t_{\text{pr}}) \sum_{n_1, n_2} \sum_{\mathbf{k}} \frac{\delta O_{\mathbf{k}, n_1, n_2}(t)}{\delta \mathbf{A}(t)} \cdot \mathbf{E}_{\text{pr}} \\ &\quad \left\langle \hat{c}_{H', \mathbf{k}, n_1}^\dagger(t) \hat{c}_{H', \mathbf{k}, n_2}(t) \right\rangle_{t_{\text{ini}}}. \end{aligned} \quad (18)$$

Comparing Eq. 18 with Eq. 16, we get

$$\begin{aligned} \chi_2(t, t_{\text{pr}}) &= -\theta(t - t_{\text{pr}}) \sum_{n_1, n_2} \sum_{\mathbf{k}} \frac{\delta O_{\mathbf{k}, n_1, n_2}(t)}{\delta \mathbf{A}(t)} \\ &\quad \left\langle \hat{c}_{H', \mathbf{k}, n_1}^\dagger(t) \hat{c}_{H', \mathbf{k}, n_2}(t) \right\rangle_{t_{\text{ini}}}. \end{aligned} \quad (19)$$

Then, to evaluate $\chi(t, t_{\text{pr}})$, one needs to compute the time evolution of the creation and annihilation operators, $\hat{c}_{H', \mathbf{k}, n_m}^\dagger(t)$ and $\hat{c}_{H', \mathbf{k}, n_m}(t)$, appearing in Eqs. 17 and 19. According to what we have recently shown in Refs. [38, 49], using the Dynamical Projective Operatorial Approach (DPOA), such operators can be projected on their equilibrium counterparts,

$$\hat{c}_{H', \mathbf{k}, n_1}(t) = \sum_{\mathbf{k}, n_2} P_{\mathbf{k}, n_1, n_2}(t) \hat{c}_{\mathbf{k}, n_2} \quad (20)$$

and the projection coefficients, $P_{\mathbf{k}, n_1, n_2}(t)$, are obtained from the following equation of motion

$$i\hbar \partial_t P_{\mathbf{k}, n_1, n_2}(t) = \sum_{n_3} h'_{\mathbf{k}, n_1, n_3}(t) P_{\mathbf{k}, n_3, n_2}(t), \quad (21)$$

with the initial condition $P_{\mathbf{k}, n_1, n_2}(t_{\text{ini}}) = \delta_{n_1, n_2}$. Using such projection coefficients and assuming that the equilibrium Hamiltonian, \hat{H}_0 , is diagonal in the basis we have chosen, i.e., $\hat{H}_0 = \sum_{\mathbf{k}, n} \varepsilon_{\mathbf{k}, n} \hat{c}_{\mathbf{k}, n}^\dagger \hat{c}_{\mathbf{k}, n}$, one can compute the two components of the response function as

$$\begin{aligned} \chi_1(t, t_{\text{pr}}) &= -\frac{i}{\hbar} \theta(t - t_{\text{pr}}) \sum_{n_1, n_2, n_3, n_4} \sum_{n'_1, n'_2} \sum_{\mathbf{k}} \hat{O}_{\mathbf{k}, n_1, n_2}(t) \int_{t_{\text{ini}}}^t dt' \sum_{\nu_1 \nu_2} \Omega_{\mathbf{k} \nu_1 n_1}^* \tilde{T}_{\mathbf{k}, \nu_1 \nu_2} \Omega_{\mathbf{k} \nu_2 n_2} = \varepsilon_{\mathbf{k}, n} \delta_{n_1 n_2}, \quad (25) \\ &\quad \left(-\frac{e}{\hbar} \mathbf{V}_{\mathbf{k}, n_3, n_4}(t') \theta(t' - t_{\text{pr}}) + e \mathbf{D}_{\mathbf{k}, n_3, n_4}(t_{\text{pr}}) \delta(t' - t_{\text{pr}}) \right) \\ &\quad P_{\mathbf{k}, n_1, n'_1}^*(t) P_{\mathbf{k}, n_2, n'_2}(t) P_{\mathbf{k}, n_3, n'_2}^*(t') P_{\mathbf{k}, n_4, n'_1}(t') (f_{\mathbf{k}, n'_1} - f_{\mathbf{k}, n'_2}), \end{aligned} \quad (22)$$

and

$$\begin{aligned} \chi_2(t, t_{\text{pr}}) &= -\theta(t - t_{\text{pr}}) \\ &\quad \sum_{n_1, n_2, n_3} \sum_{\mathbf{k}} \frac{\delta O_{\mathbf{k}, n_1, n_2}(t)}{\delta \mathbf{A}(t)} P_{\mathbf{k}, n_1, n_3}^*(t) P_{\mathbf{k}, n_2, n_3}(t) f_{\mathbf{k}, n_3}, \end{aligned} \quad (23)$$

where we have used $\left\langle \hat{c}_{\mathbf{k}, n_1}^\dagger \hat{c}_{\mathbf{k}, n_2} \right\rangle_{t_{\text{ini}}} = \delta_{n_1, n_2} f_{\mathbf{k}, n_1}$ and $\left\langle \left[\hat{c}_{\mathbf{k}, n_1}^\dagger c_{\mathbf{k}, n_2}, \hat{c}_{\mathbf{k}, n_3}^\dagger c_{\mathbf{k}, n_4} \right] \right\rangle_{t_{\text{ini}}} = \delta_{n_1, n_4} \delta_{n_2, n_3} (f_{\mathbf{k}, n_1} - f_{\mathbf{k}, n_2})$. $f_{\mathbf{k}, n} = \frac{1}{e^{(\varepsilon_{\mathbf{k}, n} - \mu)/k_B T} + 1}$ is the Fermi function that determines the equilibrium distribution of electrons in which k_B is the Boltzmann constant, T is the temperature, and μ is the chemical potential.

C. Optical conductivity

For a lattice system, in the dipole gauge, the matter-field coupling Hamiltonian, given a generic electromagnetic pulse, reads as (see Refs. [49, 50])

$$\begin{aligned} \hat{H} \{ \mathbf{A}(t), \mathbf{E}(t) \} &= \sum_{\nu_1, \nu_2, \mathbf{k}} \hat{c}_{\mathbf{k}, \nu_1}^\dagger \tilde{T}_{\mathbf{k} + \frac{e}{\hbar} \mathbf{A}(t), \nu_1, \nu_2} \hat{c}_{\mathbf{k}, \nu_2} \\ &\quad + e \mathbf{E}(t) \cdot \sum_{\nu_1 \nu_2 \mathbf{k}} \hat{c}_{\mathbf{k} \nu_1}^\dagger \tilde{\mathbf{D}}_{\mathbf{k} + \frac{e}{\hbar} \mathbf{A}(t), \nu_1 \nu_2} \hat{c}_{\mathbf{k} \nu_2}, \end{aligned} \quad (24)$$

where $\mathbf{A}(t)$ is the vector potential and $\mathbf{E}(t) = -\partial_t \mathbf{A}(t)$ is the electric field. ν_1 and ν_2 are sets of quantum numbers identifying orthogonal localized states (e.g., the maximally localized Wannier states). We neglect the coupling of the spin magnetic moments to the magnetic field of the applied pulses. $\tilde{T}_{\mathbf{k}, \nu_1 \nu_2}$ is the matrix element of the equilibrium Hamiltonian, i.e., $\hat{H}_0 = \sum_{\nu_1 \nu_2 \mathbf{k}} \hat{c}_{\mathbf{k} \nu_1}^\dagger \tilde{T}_{\mathbf{k}, \nu_1 \nu_2} \hat{c}_{\mathbf{k} \nu_2}$, and $\tilde{\mathbf{D}}_{\mathbf{k}, \nu_1 \nu_2}$ is the matrix element of the local dipole in the reciprocal space. In the absence of the probe pulse, the electric field and the vector potential are just those of the pump pulse, i.e., $\mathbf{A}_{\text{pu}}(t)$ and $\mathbf{E}_{\text{pu}}(t)$, respectively. Consequently, the Hamiltonian of the pumped system is given by $\hat{H}'(t) = \hat{H} \{ \mathbf{A}_{\text{pu}}(t), \mathbf{E}_{\text{pu}}(t) \}$.

Instead of working in the localized-state basis (ν indexed), we prefer to perform the calculations in the basis which diagonalizes the equilibrium Hamiltonian (n indexed). Using the diagonalization matrix $\Omega_{\mathbf{k}}$,

we can rewrite $\hat{H}'(t)$ as

$$\begin{aligned} \hat{H}'(t) &= \sum_{n_1 n_2 \mathbf{k}} \hat{c}_{\mathbf{k} n_1}^\dagger T_{\mathbf{k}, n_1 n_2}(t) \hat{c}_{\mathbf{k} n_2} \\ &\quad + e \mathbf{E}(t) \cdot \sum_{n_1 n_2 \mathbf{k}} \hat{c}_{\mathbf{k} n_1}^\dagger \mathbf{D}_{\mathbf{k}, n_1 n_2}(t) \hat{c}_{\mathbf{k} n_2}, \end{aligned} \quad (26)$$

where $\hat{c}_{\mathbf{k} n}^\dagger = \sum_{\nu} \hat{c}_{\mathbf{k} \nu}^\dagger \Omega_{\mathbf{k} \nu n}$. Moreover, $T_{\mathbf{k}, n_1 n_2}(t) = T_{\mathbf{k}, n_1 n_2} \{ \mathbf{A}_{\text{pu}}(t) \}$ in which

$$T_{\mathbf{k}, n_1 n_2} \{ \mathbf{A}(t) \} = \sum_{\nu_1 \nu_2} \Omega_{\mathbf{k} \nu_1 n_1}^* \tilde{T}_{\mathbf{k} + \frac{e}{\hbar} \mathbf{A}(t), \nu_1 \nu_2} \Omega_{\mathbf{k} \nu_2 n_2}, \quad (27)$$

and $\mathbf{D}_{\mathbf{k},n_1n_2}(t) = \mathbf{D}_{\mathbf{k},n_1n_2} \{ \mathbf{A}_{\text{pu}}(t) \}$ in which

$$\mathbf{D}_{\mathbf{k},n_1n_2} \{ \mathbf{A}(t) \} = \sum_{\nu_1\nu_2} \Omega_{\mathbf{k}\nu_1n_1}^* \tilde{\mathbf{D}}_{\mathbf{k}+\frac{e}{\hbar}\mathbf{A}(t),\nu_1\nu_2} \Omega_{\mathbf{k}\nu_2n_2}. \quad (28)$$

In the presence of both pump and probe pulses, the actual applied fields are given by $\mathbf{A}_{\text{pu}}(t) + \mathbf{A}_{\text{pr}}(t)$ and $\mathbf{E}_{\text{pu}}(t) + \mathbf{E}_{\text{pr}}(t)$. As discussed above, the probe pulse intensity is relatively weak and we are considering it within the linear response theory. Therefore, in order to obtain the coupling Hamiltonian between the system and the probe pulse, $\hat{H}''(t)$, we expand the full Hamiltonian, $\hat{H} \{ \mathbf{A}_{\text{pu}}(t) + \mathbf{A}_{\text{pr}}(t), \mathbf{E}_{\text{pu}}(t) + \mathbf{E}_{\text{pr}}(t) \}$, up to the linear order in the probe-pulse fields and subtract $\hat{H}'(t)$. It is worth noticing that we do not need to expand in terms of $\mathbf{E}_{\text{pr}}(t)$ as it only appears already at the linear order. Following this procedure, it's straightforward to show that $\hat{H}''(t)$ is of the form given in Eq. 10, with $\mathbf{D}_{\mathbf{k},n_1n_2}(t) = \mathbf{D}_{\mathbf{k},n_1n_2} \{ \mathbf{A}_{\text{pu}}(t) \}$ (see Eq. 28), and $\mathbf{V}_{\mathbf{k},n_1n_2}(t) = \mathbf{V}_{\mathbf{k},n_1n_2} \{ \mathbf{A}_{\text{pu}}(t), \mathbf{E}_{\text{pu}}(t) \}$, where

$$\mathbf{V}_{\mathbf{k},n_1n_2} \{ \mathbf{A}(t), \mathbf{E}(t) \} = \boldsymbol{\eta}_{\mathbf{k},n_1n_2} \{ \mathbf{A}(t) \} + e \boldsymbol{\Lambda}_{\mathbf{k},n_1n_2} \{ \mathbf{A}(t) \} \cdot \mathbf{E}(t), \quad (29)$$

in which

$$\boldsymbol{\eta}_{\mathbf{k},n_1n_2} \{ \mathbf{A}(t) \} = \sum_{\nu_1\nu_2} \Omega_{\mathbf{k}\nu_1n_1}^* \left[\nabla_{\mathbf{k}} \tilde{\mathbf{T}}_{\mathbf{k}+\frac{e}{\hbar}\mathbf{A}(t),\nu_1\nu_2} \right] \Omega_{\mathbf{k}\nu_2n_2}, \quad (30)$$

is proportional to the velocity at the crystal momentum $\mathbf{k} + \frac{e}{\hbar}\mathbf{A}(t)$ transformed to the equilibrium diagonal basis at the crystal momentum \mathbf{k} . Moreover,

$$\boldsymbol{\Lambda}_{\mathbf{k},n_1n_2} \{ \mathbf{A}(t) \} = \sum_{\nu_1\nu_2} \Omega_{\mathbf{k}\nu_1n_1}^* \left[\nabla_{\mathbf{k}} \tilde{\mathbf{D}}_{\mathbf{k}+\frac{e}{\hbar}\mathbf{A}(t),\nu_1\nu_2} \right] \Omega_{\mathbf{k}\nu_2n_2}, \quad (31)$$

is a rank 2 tensor with the first index in momentum space coordinates (coming from $\nabla_{\mathbf{k}}$) and the second index in direct space ones (coming from $\tilde{\mathbf{D}}_{\mathbf{k},\nu_1\nu_2}$). This latter is the one saturated by the scalar product with the electric field.

The optical conductivity is the response function describing how an electric current is induced by the probe pulse. The zero-momentum particle current (i.e., the particle current integrated over the pulse-interacting portion of the volume of the sample), in the presence of the pump field and in the dipole gauge is given by (see Refs. [49, 50]) $\hat{\mathbf{J}}(t) = \hat{\mathbf{J}} \{ \mathbf{A}_{\text{pu}}(t) \}$ where

$$\hat{\mathbf{J}} \{ \mathbf{A}(t) \} = \sum_{n_1n_2\mathbf{k}} \hat{c}_{\mathbf{k}n_1}^\dagger \mathbf{J}_{\mathbf{k},n_1n_2} \{ \mathbf{A}(t) \} \hat{c}_{\mathbf{k}n_2}, \quad (32)$$

in which

$$\mathbf{J}_{\mathbf{k},n_1n_2} \{ \mathbf{A}(t) \} = \frac{1}{\hbar} \boldsymbol{\eta}_{\mathbf{k},n_1n_2} \{ \mathbf{A}(t) \} - \frac{i}{\hbar} [\mathbf{D}_{\mathbf{k}} \{ \mathbf{A}(t) \}, \mathbf{T}_{\mathbf{k}} \{ \mathbf{A}(t) \}]_{n_1n_2}, \quad (33)$$

where $[\Phi, \Psi]_{n_1n_2} = \sum_{n'} (\Phi_{n_1n'} \Psi_{n'n_2} - \Psi_{n_1n'} \Phi_{n'n_2})$.

The macroscopic particle current, which is the averaged microscopic particle current over a macroscopic number of unit cells, is just the zero-momentum current divided by the pulse-interacting portion of the volume of the sample, \mathcal{V} . Therefore, the macroscopic electric current, or simply the electric current, is $-e\hat{\mathbf{J}}(t)/\mathcal{V}$. Using Eq. 22, with $\hat{O}(t) = -e\hat{\mathbf{J}}(t)/\mathcal{V}$, the first component of optical conductivity is obtained as

$$\begin{aligned} \sigma_1(t, t_{\text{pr}}) = & \frac{ie}{\hbar\mathcal{V}} \theta(t - t_{\text{pr}}) \sum_{\mathbf{k}} \sum_{n_1n_2n_3n_4} \sum_{n'_1n'_2} \mathbf{J}_{\mathbf{k},n_1n_2}(t) \int_{t_{\text{ini}}}^t dt' \\ & \left(-\frac{e}{\hbar} \mathbf{V}_{\mathbf{k},n_3n_4}(t') \theta(t' - t_{\text{pr}}) + e \mathbf{D}_{\mathbf{k},n_3n_4}(t') \delta(t' - t_{\text{pr}}) \right) \\ & P_{\mathbf{k}n_1n'_1}^*(t) P_{\mathbf{k}n_2n'_2}(t) P_{\mathbf{k}n_3n'_2}^*(t') P_{\mathbf{k}n_4n'_1}(t') (f_{\mathbf{k}n'_1} - f_{\mathbf{k}n'_2}). \end{aligned} \quad (34)$$

For the second component of the optical conductivity, we have

$$\sigma_2(t, t_{\text{pr}}) = \frac{e}{\mathcal{V}} \theta(t - t_{\text{pr}}) \sum_{n_1n_2\mathbf{k}} \frac{\delta \mathbf{J}_{\mathbf{k},n_1n_2}(t)}{\delta \mathbf{A}(t)} N_{\mathbf{k}n_1n_2}(t), \quad (35)$$

where

$$N_{\mathbf{k}n_1n_2}(t) = \sum_{n'} P_{\mathbf{k}n_1n'}^*(t) P_{\mathbf{k}n_2n'}(t) f_{\mathbf{k}n'}, \quad (36)$$

and

$$\begin{aligned} \frac{\delta \mathbf{J}_{\mathbf{k},n_1n_2}(t)}{\delta \mathbf{A}(t)} = & \frac{e}{\hbar^2} \boldsymbol{\xi}_{\mathbf{k},n_1n_2}(t) \\ & - \frac{ie}{\hbar^2} [\boldsymbol{\Lambda}_{\mathbf{k}}(t), \mathbf{T}_{\mathbf{k}}(t)]_{n_1n_2} - \frac{ie}{\hbar^2} [\mathbf{D}_{\mathbf{k}}(t), \boldsymbol{\eta}_{\mathbf{k}}(t)]_{n_1n_2}, \end{aligned} \quad (37)$$

in which $\boldsymbol{\Lambda}_{\mathbf{k}}(t) = \boldsymbol{\Lambda}_{\mathbf{k}} \{ \mathbf{A}_{\text{pu}}(t) \}$, $\boldsymbol{\eta}_{\mathbf{k},n_1n_2}(t) = \boldsymbol{\eta}_{\mathbf{k},n_1n_2} \{ \mathbf{A}_{\text{pu}}(t) \}$, and $\boldsymbol{\xi}_{\mathbf{k},n_1n_2}(t) = \boldsymbol{\xi}_{\mathbf{k},n_1n_2} \{ \mathbf{A}_{\text{pu}}(t) \}$ where

$$\boldsymbol{\xi}_{\mathbf{k},n_1n_2} \{ \mathbf{A}(t) \} = \sum_{\nu_1\nu_2} \Omega_{\mathbf{k}\nu_1n_1}^* \left[\nabla_{\mathbf{k}}^2 \tilde{\mathbf{T}}_{\mathbf{k}+\frac{e}{\hbar}\mathbf{A}(t),\nu_1\nu_2} \right] \Omega_{\mathbf{k}\nu_2n_2}, \quad (38)$$

is proportional to the inverse-mass tensor at the crystal momentum $\mathbf{k} + \frac{e}{\hbar}\mathbf{A}(t)$ transformed to the equilibrium diagonal basis at the crystal momentum \mathbf{k} .

The total optical conductivity is thus obtained by adding up its two components as,

$$\boldsymbol{\sigma}(t, t_{\text{pr}}) = \boldsymbol{\sigma}_1(t, t_{\text{pr}}) + \boldsymbol{\sigma}_2(t, t_{\text{pr}}). \quad (39)$$

We choose the center of the pump pulse envelope as the origin of the time axis. Accordingly, t_{pr} is just the time

delay between pump and probe pulses. One is usually interested in the optical conductivity in terms of frequency and time delay, which is obtained by performing a Fourier transformation with respect to $t - t_{\text{pr}}$, i.e.,

$$\boldsymbol{\sigma}(\omega, t_{\text{pr}}) = \int_{-\infty}^{+\infty} e^{i(\omega+i0^+)(t-t_{\text{pr}})} \boldsymbol{\sigma}(t, t_{\text{pr}}) dt, \quad (40)$$

where 0^+ is a small damping factor.

D. Reflectivity and Absorption

In this section, we consider the absorption and the reflectivity, which are the optical quantities usually measured in real experimental setups. Let us consider that the electric field of the probe pulse is polarized along some specific direction determined by the unit vector $\boldsymbol{\lambda}_{\text{pr}}$, and its reflection is measured along the direction $\boldsymbol{\lambda}'_{\text{pr}}$. Therefore, the relevant element of our optical conductivity tensor would be $\boldsymbol{\lambda}'_{\text{pr}} \cdot \boldsymbol{\sigma}(\omega, t_{\text{pr}}) \cdot \boldsymbol{\lambda}_{\text{pr}}$. We assume that the off-diagonal elements of the optical conductivity tensor are negligible, i.e., the only relevant case to be studied is $\boldsymbol{\lambda}_{\text{pr}} = \boldsymbol{\lambda}'_{\text{pr}}$. It is worth noting that if the spin inversion symmetry is not broken, one can consider only one spin direction in the calculations and just double the final result for the optical conductivity.

From the optical conductivity one can obtain the dielectric function, $\epsilon(\omega, t_{\text{pr}})$, as (see App. B)

$$\epsilon(\omega, t_{\text{pr}}) = 1 + \frac{i}{\omega\epsilon_0} \sigma(\omega, t_{\text{pr}}), \quad (41)$$

where ϵ_0 is the vacuum dielectric constant, $\sigma(\omega, t_{\text{pr}}) = \boldsymbol{\lambda}_{\text{pr}} \cdot \boldsymbol{\sigma}(\omega, t_{\text{pr}}) \cdot \boldsymbol{\lambda}_{\text{pr}}$, and $\epsilon(\omega, t_{\text{pr}}) = \boldsymbol{\lambda}_{\text{pr}} \cdot \boldsymbol{\epsilon}(\omega, t_{\text{pr}}) \cdot \boldsymbol{\lambda}_{\text{pr}}$.

As discussed in App. B, when the probe pulse frequency is much larger than the pump pulse one, one can use the well-known formula for equilibrium reflectivity also to obtain the reflectivity out of equilibrium. Then, for a s-polarized probe pulse at an incident angle θ , with frequency ω and center t_{pr} , the transient reflectivity is given by

$$R_\theta(\omega, t_{\text{pr}}) = \left| \frac{\cos\theta - \sqrt{\epsilon(\omega, t_{\text{pr}}) - \sin^2\theta}}{\cos\theta + \sqrt{\epsilon(\omega, t_{\text{pr}}) - \sin^2\theta}} \right|^2. \quad (42)$$

To analyze the experimental results [38], we are interested in the transient relative differential reflectivity, $\delta_r R_\theta(\omega, t_{\text{pr}})$, defined as

$$\delta_r R_\theta(\omega, t_{\text{pr}}) = \frac{R_\theta(\omega, t_{\text{pr}}) - R_\theta^{\text{eq}}(\omega)}{R_\theta^{\text{eq}}(\omega)}, \quad (43)$$

where $R_\theta^{\text{eq}}(\omega) = R_\theta(\omega, t_{\text{pr}} \rightarrow t_{\text{ini}})$ is the equilibrium reflectivity computed using the optical conductivity given in Eq. 47.

To get more insight into the transient reflectivity and its frequency content, one may perform a Fourier transform with respect to the time t_{pr} and obtain

$$\delta_r R_\theta(\omega, \omega') = \int_{-\infty}^{+\infty} e^{i\omega t_{\text{pr}}} \delta_r R_\theta(\omega, t_{\text{pr}}) dt_{\text{pr}}. \quad (44)$$

Another interesting optical property is the absorption coefficient, which is given by

$$\alpha(\omega, t_{\text{pr}}) = \frac{\omega}{n_{\text{refr}}(\omega, t_{\text{pr}})c} \text{Im}[\epsilon(\omega, t_{\text{pr}})], \quad (45)$$

where c is the speed of light in vacuum and $n_{\text{refr}}(\omega, t_{\text{pr}}) = \text{Re}[\sqrt{\epsilon(\omega, t_{\text{pr}})}]$ is the real transient refractive index. In our numerical calculations, in order to study the transient behavior of the system, we will investigate the transient differential absorption coefficient,

$$\delta\alpha(\omega, t_{\text{pr}}) = \alpha(\omega, t_{\text{pr}}) - \alpha^{\text{eq}}(\omega), \quad (46)$$

where $\alpha^{\text{eq}}(\omega)$ is the absorption coefficient at equilibrium.

E. Equilibrium properties

In equilibrium, we have $P_{\mathbf{k},nn'}(t) = e^{-i\omega_{\mathbf{k}n}(t-t_{\text{ini}})} \delta_{nn'}$. Inserting this into Eqs. 34 and 35, and performing some straightforward calculations, one obtains

$$\boldsymbol{\sigma}^{\text{eq}}(\omega) = \boldsymbol{\sigma}^{\text{eq,main}}(\omega) + \boldsymbol{\sigma}_1^{\text{eq,tail}}(\omega) + \boldsymbol{\sigma}_2^{\text{eq,tail}}(\omega), \quad (47)$$

where

$$\boldsymbol{\sigma}^{\text{eq,main}}(\omega) = \frac{ie^2}{\hbar\mathcal{V}} \sum_{\mathbf{k}} \sum_{nn'} \frac{\mathbf{J}_{\mathbf{k},n'n} \mathbf{J}_{\mathbf{k},nn'} (f_{\mathbf{k},n'} - f_{\mathbf{k},n})}{\omega_{\mathbf{k},nn'} (\omega - \omega_{\mathbf{k},nn'} + i0^+)}, \quad (48)$$

and

$$\boldsymbol{\sigma}_1^{\text{eq,tail}}(\omega) = -\frac{ie^2}{\hbar^3\mathcal{V}} \sum_{\mathbf{k}} \sum_{nn'} \frac{\boldsymbol{\eta}_{\mathbf{k},n'n} \boldsymbol{\eta}_{\mathbf{k},nn'} (f_{\mathbf{k},n'} - f_{\mathbf{k},n})}{\omega_{\mathbf{k}nn'} (\omega + i0^+)}, \quad (49)$$

and

$$\boldsymbol{\sigma}_2^{\text{eq,tail}}(\omega) = \frac{ie^2}{\hbar^2\mathcal{V}} \sum_{\mathbf{k}} \sum_{nn'} \frac{f_{\mathbf{k},n} \boldsymbol{\xi}_{\mathbf{k},nn'} \delta_{nn'}}{\omega + i0^+}, \quad (50)$$

in which $\omega_{\mathbf{k},nn'} = \omega_{\mathbf{k},n} - \omega_{\mathbf{k},n'} = (\varepsilon_{\mathbf{k},n} - \varepsilon_{\mathbf{k},n'})/\hbar$, and $\mathbf{J}_{\mathbf{k},nn'} = \mathbf{J}_{\mathbf{k},nn'}(t \rightarrow t_{\text{ini}}) = \boldsymbol{\eta}_{\mathbf{k},nn'}/\hbar + i\omega_{\mathbf{k},nn'} \mathbf{D}_{\mathbf{k},nn'}$.

$\boldsymbol{\sigma}^{\text{eq,main}}(\omega)$ is the main contribution to the equilibrium conductivity, which doesn't diverge in the limit $\omega \rightarrow 0$ (see below). On the other hand, $\boldsymbol{\sigma}^{\text{eq,tail}}(\omega) =$

$\sigma_1^{\text{eq,tail}}(\omega \rightarrow 0) + \sigma_2^{\text{eq,tail}}(\omega \rightarrow 0)$ in general diverges in the static limit, $\omega \rightarrow 0$, which gives the expected Drude behavior. However, for semiconductors at zero temperature, one can show that $\sigma_1^{\text{eq,tail}}(\omega \rightarrow 0) = -\sigma_2^{\text{eq,tail}}(\omega \rightarrow 0)$ and, therefore, $\sigma^{\text{eq,tail}}(\omega)$ identically vanishes (see App. D). In numerical calculations for *real* materials, the relative difference of $\sigma_1^{\text{eq,tail}}(\omega \rightarrow 0)$ and $-\sigma_2^{\text{eq,tail}}(\omega \rightarrow 0)$ can be used to check if the adopted \mathbf{k} grid is dense enough and/or if the number of energy bands taken into account is sufficient.

After this discussion on the optical conductivity, it is relevant to study the behavior of the equilibrium dielectric function in the static limit, $\omega \rightarrow 0$. For the sake of simplicity, we consider zero temperature, so that the tails in the optical conductivity cancel each other and we get $\sigma^{\text{eq}}(\omega) \rightarrow \sigma^{\text{eq,main}}(\omega)$, where $\sigma^{\text{eq}}(\omega) = \boldsymbol{\lambda}_{\text{pr}} \cdot \boldsymbol{\sigma}^{\text{eq}}(\omega) \cdot \boldsymbol{\lambda}_{\text{pr}}$. After some tricky calculations, one can show that the static limit of the equilibrium dielectric function is given by

$$\epsilon^{\text{eq}}(\omega \rightarrow 0) = 1 + \left(1 + i \frac{0^+}{\omega}\right) C, \quad (51)$$

where

$$C = \frac{e^2}{\hbar \epsilon_0 \mathcal{V}} \sum_{\mathbf{k}} \sum_{nn'} \frac{|J_{\mathbf{k},n'n}|^2}{\omega_{\mathbf{k},nn'}^3} (f_{\mathbf{k},n'} - f_{\mathbf{k},n}), \quad (52)$$

in which $J_{\mathbf{k},n'n} = \boldsymbol{\lambda}_{\text{pr}} \cdot \mathbf{J}_{\mathbf{k},n'n}$. C is in general a real positive number, so that the static dielectric function is larger than 1, as it is quite well known for semiconductors. The imaginary part of $\epsilon^{\text{eq}}(\omega \rightarrow 0)$ is given by $\frac{0^+}{\omega} C$, which vanishes if one takes the correct order of the limits: first $0^+ \rightarrow 0$ and then $\omega \rightarrow 0$. In numerical calculations, at low frequencies, 0^+ is a finite number and $\frac{0^+}{\omega}$ cannot vanish in the limit of $\omega \rightarrow 0$. Actually, our results are valid only if the probe frequency is much larger than 0^+ . As we will describe below, in order to have a smaller 0^+ , one needs a higher energy resolution and consequently a finer grid in \mathbf{k} space. This is consistent with the fact that, to study the behavior of a system in some energy regime, it is needed a sufficiently fine energy resolution of the energy spectrum of the system.

Having computed the optical conductivity, one can obtain the dielectric function in equilibrium and in turn, the real refractive index in equilibrium. For the frequencies where the real equilibrium refractive index, $n_{\text{refr}}^{\text{eq}}(\omega)$, is smaller than 1, one can define the critical incident angle, $\theta_C(\omega)$, as

$$\theta_C(\omega) = \sin^{-1} [n_{\text{refr}}^{\text{eq}}(\omega)]. \quad (53)$$

In absence of absorption, for incident angles above $\theta_C(\omega)$, we have total external reflection, i.e., the reflectivity is equal to 1. In presence of absorption, the reflectivity is smaller than 1 even for incident angles above $\theta_C(\omega)$. On the other hand, for $n_{\text{refr}}^{\text{eq}}(\omega) \geq 1$ we have $\theta_C(\omega) = 90^\circ$.

F. Guidelines for numerical calculations

In this section, we give some guidelines that can help to perform the numerical calculations of the reflectivity and of the absorption in different pump-probe setups.

1. Rewriting the expression for the optical conductivity to simplify its numerical calculation

At a first glance, it may seem that Eq. 34 is computationally very expensive. It requires summing over many indices and this can be quite heavy for *real* materials. Moreover, one has to calculate a time integral for each pair of t and t_{pr} . However, with some careful manipulations, these complexities can be simplified. One can rewrite Eq. 34 as follows

$$\sigma_1(t, t_{\text{pr}}) = \frac{ie}{\hbar \mathcal{V}} \theta(t - t_{\text{pr}}) \sum_{\mathbf{k}} \text{Tr} \{ Z_{\mathbf{k}}(t) \circ [Y_{\mathbf{k}}(t) - Y_{\mathbf{k}}(t_{\text{pr}}) + X_{\mathbf{k}}(t_{\text{pr}})] \}, \quad (54)$$

where \circ stands for the matrix product in the band space and $Z_{\mathbf{k}}(t)$, $Y_{\mathbf{k}}(t)$ and $X_{\mathbf{k}}(t)$ are matrices with the following elements:

$$Z_{\mathbf{k},n'_1n'_2}(t) = \sum_{n_1n_2} \mathbf{J}_{\mathbf{k},n_1n_2}(t) P_{\mathbf{k},n_1n'_1}^*(t) P_{\mathbf{k},n_2n'_2}(t) (f_{\mathbf{k}n'_1} - f_{\mathbf{k}n'_2}), \quad (55)$$

$$Y_{\mathbf{k},n'_2n'_1}(t) = -\frac{e}{\hbar} \sum_{n_3n_4} \int_{t_{\text{ini}}}^t dt' \mathbf{V}_{\mathbf{k},n_3n_4}(t') P_{\mathbf{k},n_3n'_2}^*(t') P_{\mathbf{k},n_4n'_1}(t'), \quad (56)$$

$$X_{\mathbf{k},n'_2n'_1}(t) = e \sum_{n_3n_4} \mathbf{D}_{\mathbf{k},n_3n_4}(t) P_{\mathbf{k},n_3n'_2}^*(t) P_{\mathbf{k},n_4n'_1}(t). \quad (57)$$

Using such matrices, the numerical calculations of $\sigma_1(t, t_{\text{pr}})$ becomes very fast and efficient.

It is worth noting that, in the numerical calculations, where it is obviously needed to discretize the t time axis, at each step of time, t_m , one can compute $Y_{\mathbf{k},n'_2n'_1}(t_m)$ (Eq. 56) recursively from $Y_{\mathbf{k},n'_2n'_1}(t_{m-1})$ and approximating the remaining integral between t_{m-1} and t_m . Therefore, there is no need to perform the increasingly expensive integration between t_{ini} and t_m for each t_m .

2. Finite numerical momentum grid and corresponding damping factor

For the numerical calculations, we need to consider a finite grid in the first Brillouin zone to sample the momentum \mathbf{k} . Such a grid will have a total number of \mathbf{k}

points N_{grid} and all summations over \mathbf{k} should be performed as $\frac{1}{V} \sum_{\mathbf{k}} \rightarrow \frac{1}{v_{\text{uc}} N_{\text{grid}}} \sum_{\mathbf{k} \in \text{grid}}$ where v_{uc} is the unit cell volume. Another issue which is directly connected to the numerical \mathbf{k} grid is the finite damping factor, or equivalently, level broadening, 0^+ . In real experimental setups, one always deals with a finite level broadening originating from several scattering mechanisms (such as electron-phonon interaction, disorder, etc.) present in the system, or even from the measurement procedure. Such a level broadening brings a finite energy resolution, which justifies the use of a finite momentum grid instead of the almost continuous *real* one. The sparser is the \mathbf{k} grid, implying a lower and lower achievable energy resolution, the larger has to be the value of 0^+ . This is crucial in the numerical calculations: if the value of 0^+ is smaller than the band energy resolution provided by the momentum grid, the features corresponding to individual \mathbf{k} points show up in the final results making them artificially spiky. Then, if one is forced, by the available computational resources, to use a sparser \mathbf{k} grid than the one consistent with the actual damping in the *real* material under analysis (as it is usually the case), one has to use a larger value of 0^+ than the physical one and this comes at the cost of suppressing possibly relevant physical features (see App. F).

3. Analytical simplification regarding the time range after the application of the pump pulse

The time step for the Fourier transformation of the optical conductivity, Eq. 40, should be small enough so that its reciprocal is larger than the frequency of the probe pulse. On the other hand, the values of t_{pr} suffer no physical or mathematical restrictions, and one can freely choose the instants of time at which to probe the system. The initial time in the numerical calculations, $t_{\text{ini}} \rightarrow -\infty$, is simple to choose: it should be a time where the pump pulse is negligible, and also should meet the criteria $t_{\text{ini}} < t_{\text{pr}}$.

However, for the final time, $t_{\text{fin}} \rightarrow +\infty$, in addition to the condition that the pump pulse should become negligible after its application and that $t_{\text{fin}} > t_{\text{pr}}$ for every t_{pr} , it is needed that the integrand of Eq. 40 becomes negligible at t_{fin} . That is, for every t_{pr} , it is required that $e^{-0^+(t_{\text{fin}}-t_{\text{pr}})} \simeq 0$. One can always choose a large enough value for t_{fin} and solve this problem. However, in order to increase the speed of computations, one can choose t_{fin} to meet only one criteria, i.e., the vanishing of pump and probe pulses, and write

$$\boldsymbol{\sigma}(\omega, t_{\text{pr}}) = \bar{\boldsymbol{\sigma}}(\omega, t_{\text{pr}}) + \boldsymbol{\sigma}^{\text{a.p.}}(\omega, t_{\text{pr}}), \quad (58)$$

where the first term on the right hand side is the result of the numerical calculations

$$\bar{\boldsymbol{\sigma}}(\omega, t_{\text{pr}}) = \int_{t_{\text{pr}}}^{t_{\text{fin}}} dt e^{i(\omega+i0^+)(t-t_{\text{pr}})} \boldsymbol{\sigma}(t, t_{\text{pr}}), \quad (59)$$

while the second term, which we dub *after-pump* contribution, is given by

$$\boldsymbol{\sigma}^{\text{a.p.}}(\omega, t_{\text{pr}}) = \int_{t_{\text{fin}}}^{\infty} dt e^{i(\omega+i0^+)(t-t_{\text{pr}})} \boldsymbol{\sigma}(t, t_{\text{pr}}), \quad (60)$$

and can be calculated analytically, as we are going to describe in the following. For $t > t_{\text{fin}}$, the pump pulse becomes negligible, and the projection coefficients follow a trivial dynamics:

$$P_{\mathbf{k}nn'}(t) = e^{-i\omega_{\mathbf{k}n}(t-t_{\text{fin}})} P_{\mathbf{k}nn'}(t_{\text{fin}}), \quad t \geq t_{\text{fin}}, \quad (61)$$

and the pump-pulse dependent observable matrix elements (such as velocities, dipole elements, currents, etc.) return to their equilibrium values. After some lengthy but straightforward calculations one can show that

$$\boldsymbol{\sigma}_1^{\text{a.p.}}(\omega, t_{\text{pr}}) = -\frac{ie^2}{\hbar V} \sum_{\mathbf{k}} \{W_{\mathbf{k}}(\omega, t_{\text{fin}}, t_{\text{pr}}) + \text{Tr}[Q_{\mathbf{k}}(\omega, t_{\text{fin}}, t_{\text{pr}}) \circ S_{\mathbf{k}}(t_{\text{fin}}, t_{\text{pr}})]\}, \quad (62)$$

where

$$Q_{\mathbf{k},n'n}(\omega, t_{\text{fin}}, t_{\text{pr}}) = \sum_{n_1 n_2} P_{\mathbf{k},n_2 n'}^*(t_{\text{fin}}) \mathbf{J}_{\mathbf{k},n_3 n_4} P_{\mathbf{k},n_1 n}(t_{\text{fin}}) \frac{ie^{(i\omega-0^+)(t_{\text{fin}}-t_{\text{pr}})}}{(\omega - \omega_{\mathbf{k}}^{n_1 n_2} + i0^+)} (f_{\mathbf{k}n'} - f_{\mathbf{k}n}), \quad (63)$$

$$S_{\mathbf{k}}(t_{\text{fin}}, t_{\text{pr}}) = Y_{\mathbf{k}}(t_{\text{fin}}) - Y_{\mathbf{k}}(t_{\text{pr}}) - X_{\mathbf{k}}(t_{\text{pr}}), \quad (64)$$

$$W_{\mathbf{k}}(\omega, t_{\text{fin}}, t_{\text{pr}}) = -\frac{1}{\hbar} \sum_{n_1 n_2} \frac{e^{(i\omega-0^+)(t_{\text{fin}}-t_{\text{pr}})} \mathbf{J}_{\mathbf{k},n_2 n_1}}{\omega - \omega_{\mathbf{k}}^{n_1 n_2} + i0^+} \sum_n \left(\frac{\boldsymbol{\eta}_{\mathbf{k},n_1 n}}{\omega - \omega_{\mathbf{k}}^{n_2 n} + i0^+} N_{\mathbf{k},n_2 n}(t_{\text{fin}}) - \frac{\boldsymbol{\eta}_{\mathbf{k},nn_2}}{\omega - \omega_{\mathbf{k}}^{n_1 n} + i0^+} N_{\mathbf{k},nn_1}(t_{\text{fin}}) \right), \quad (65)$$

and

$$\boldsymbol{\sigma}_2^{\text{a.p.}}(\omega, t_{\text{pr}}) = \frac{e}{V} \sum_{\mathbf{k}} \sum_{n_1 n_2} \frac{iN_{\mathbf{k},n_1 n_2}(t_{\text{fin}}) \frac{\delta \mathbf{J}_{\mathbf{k},n_1 n_2}}{\delta \mathbf{A}}}{\omega_{\mathbf{k},n_1 n_2} + \omega + i0^+}, \quad (66)$$

and clearly, we have

$$\boldsymbol{\sigma}^{\text{a.p.}}(\omega, t_{\text{pr}}) = \boldsymbol{\sigma}_1^{\text{a.p.}}(\omega, t_{\text{pr}}) + \boldsymbol{\sigma}_2^{\text{a.p.}}(\omega, t_{\text{pr}}). \quad (67)$$

4. Approximations considering the core levels

Another numerical efficiency improvement can be achieved by separating the *core* bands, which are far below the Fermi energy (i.e., the energy gaps between them

and the other bands are out of resonance by far with respect to the pump photon energy), from the valence and the conduction bands. Obviously, the core bands are completely filled at equilibrium, i.e., $f_{\mathbf{k}n_{\text{core}}} = 1$, and we can consider negligible the effect of the pump pulse on them. Therefore, one can write

$$P_{\mathbf{k}n_{\text{core}}n}(t) = P_{\mathbf{k}nn_{\text{core}}}(t) = e^{-i\omega_{\mathbf{k}n_{\text{core}}}(t-t_{\text{ini}})}\delta_{nn_{\text{core}}}, \quad (68)$$

where $\omega_{\mathbf{k},n_{\text{core}}} = \varepsilon_{\mathbf{k},n_{\text{core}}}/\hbar$.

Another approximation regarding the *core* bands is to consider only the energy gaps between them and the valence and conduction bands in computing the optical conductivity, and neglect the contributions coming from the energy gaps between valence and conduction bands. For more details about this approximation see App. C.

5. Quasi-static approximation

Finally, a possible approximation one may think of is to assume that on the time scale corresponding to the probe frequencies, the pump-induced evolution can be considered quasi-static. Even though such an approximation speeds up the calculations, as it allows for a significant part of the job to be done analytically, it cannot reproduce some relevant features of the actual behavior of the optical properties. For further discussions about this approximation see App. E.

III. RESULTS

A. The system

In this section, we consider the minimal model for a semiconducting material: a cubic lattice with lattice constant a and one valence (VB), one conduction (CB), and one *core* band. We consider the VB and the CB to derive from two Wannier states with onsite energies $\tilde{T}_{\mathbf{0},1,1} = -1.65\Delta$ and $\tilde{T}_{\mathbf{0},2,2} = 1.35\Delta$, diagonal first-neighbor hoppings $\tilde{T}_{\mathbf{a},1,1} = 0.2\Delta$ and $\tilde{T}_{\mathbf{a},2,2} = -0.15\Delta$, and off-diagonal first-neighbor hoppings $\tilde{T}_{\mathbf{a},1,2} = \tilde{T}_{\mathbf{a},2,1} = -0.1\Delta$, where, as mentioned before, $\tilde{T}_{\mathbf{R},\nu,\nu'}$ is the hopping matrix between two Wannier states ν and ν' centered at distance \mathbf{R} , and $\mathbf{a} \in \{a(\pm 1, 0, 0), a(0, \pm 1, 0), a(0, 0, \pm 1)\}$. Δ is the unit of energy and can be adjusted to obtain the desired band-gap energies. As a reference, $\Delta = 0.5$ eV gives a band gap of 0.75 eV at Γ . The *core* band is assumed to be flat, with an energy $\varepsilon_{\text{core}} = -50\Delta$. A momentum-independent local dipole matrix element $\mathbf{D} = i0.05a\hat{\mathbf{j}}$ is considered between the *core* level and both the VB and the CB. We sample the \mathbf{k} space by a cubic grid of size $32 \times 32 \times 32$ pinned at Γ . The damping factor for computing the optical conductivity in the XUV regime is chosen to be $0^+ = 0.05\Delta/\hbar$ (see App. 9).

In Fig. 1 (left panel), we show the band energies along the main path passing through the high-symmetry points

in the \mathbf{k} space of the cubic lattice [49] as well as the one-photon sideband of the VB corresponding to a photon energy 2.33Δ . Pumping the system with such a frequency, at the \mathbf{k} -points where this sideband crosses the CB, we have the exact one-photon resonances and, therefore, Rabi-like excitations. Given a \mathbf{k} -point, pumping fields with different polarization directions couple very differently to the system because the velocity $\boldsymbol{\eta}_{\mathbf{k}}$ is direction-dependent in \mathbf{k} space.

In the middle panel of Fig. 1, we plot the critical angle, the real and imaginary parts of the dielectric function, and the absorption coefficient, in equilibrium, as functions of the probe photon energy, ω . At the moment, we are interested in the XUV regime, which we define as the range of the energy gaps between the *core* band and the VB/CB: this requires that the *real* material has at least one *core* band in the XUV energy range below the Fermi energy. According to this, the probe explores the available states in the VB and the CB by exciting electrons from the *core* band to such bands. Consequently, given that our *core* band is *flat*, every probe photon energy $\hbar\omega$ corresponds to the energy $\hbar\omega - |\varepsilon_{\text{core}}|$ in the VB/CB energies. This is implicitly understood hereafter, and every optical feature at a given XUV photon energy, $\hbar\omega$, is possibly connected to the related band energy $\varepsilon(\mathbf{k})$ after subtracting the *core* energy, $|\varepsilon_{\text{core}}|$. Accordingly, the edges of the VB (CB) are marked by dashed-wine (dotted-blue) vertical lines in all panels of Fig. 1 at the *proper* XUV photon energy, panel by panel.

$\text{Im}[\epsilon^{\text{eq}}(\omega)]$ has a behavior very similar to the absorption coefficient, $\alpha^{\text{eq}}(\omega)$, and both of them are finite only in the CB energy range. This can be understood by noting that in equilibrium, the XUV photons can be absorbed only by exciting the electrons from the *core* band to the empty states of CB. However, the finite numerical value of 0^+ gives a small broadening in $\text{Im}[\epsilon^{\text{eq}}(\omega)]$ and $\alpha^{\text{eq}}(\omega)$ outside of the energy range of the CB. One should also consider that in real systems 0^+ is finite, as several kinds of imperfections and interactions/couplings make the lifetime of the excited states finite and broaden the energy bands.

The real part of the dielectric function, $\text{Re}[\epsilon^{\text{eq}}(\omega)]$, collects contributions from each \mathbf{k} -point (Eq. 48) in the form of a Cauchy's principal part, centered at its corresponding CB energy, and therefore, outside of the energy range of the CB, $\text{Re}[\epsilon^{\text{eq}}(\omega)]$ does not vanish, and instead, has a hyperbolic-like drop vs energy with a tail that is finite even in the energy range of the VB. Even though the VB does not contribute to the optical properties at equilibrium, this tail results in a non-zero equilibrium reflectivity at the VB energy range, as discussed in the following. Generally, the non-locality in energy (long tails) of Cauchy's principal part makes some of the optical properties at each photon energy not only affected by the band structure at such energy but also by the overall band structure.

In the middle panel of Fig. 1, we also have the critical angle, θ_C . Here, we assumed the reflection of an

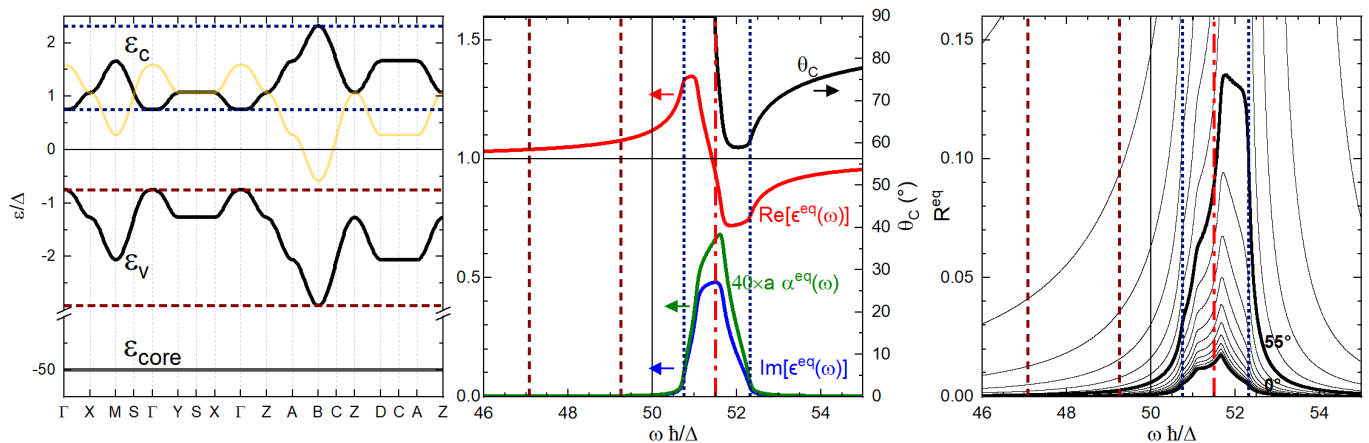


Figure 1. (left) Equilibrium bands along the main path passing through the high-symmetry points in the \mathbf{k} space of the cubic lattice. The one-photon side-band with photon energy 2.33Δ with respect to the VB is also shown (solid yellow). At the \mathbf{k} points where this side-band crosses the CB, we have one-photon resonances and Rabi-like excitations. (middle) The critical angle, the real and imaginary parts of the dielectric function, and the absorption coefficient, at equilibrium, as functions of the probe photon energy ω . The absorption coefficient has been multiplied by the lattice constant a to make it dimensionless and by 40 to make it visible on the range of the left scale. A dashed-dot vertical red line marks the frequency below which the critical angle is just 90° . (right) The equilibrium reflectivity at different incident angles, starting from 0° (normal incidence) and increasing with the steps of 5° , vs the probe photon energy ω . The top and the bottom of the VB (CB) are marked by dashed-wine (dotted-blue) lines in all panels.

s-polarized probe with an incident angle measured with respect to the normal to the sample interface. The vertical red dash-dot line shows the probe photon frequency where $\text{Re}[n_{\text{refr}}^{\text{eq}}] = 1$, so that above (below) this frequency, θ_C is less than (equal to) 90° . In the experimental setups, the incident angle of the probe is chosen to be just below the critical angle in the range of probe photon energies. This guarantees a high signal-to-noise-ratio in the reflected beam and makes the results more precise and reliable. According to this, in our case, we will choose the incident angle to be 55° .

In Fig. 1 (right panel), we show the equilibrium reflectivities vs the probe photon energy, ω , for different incident angles starting from 0° (normal incidence) and increasing in steps of 5° . The reflectivity eventually tends to zero for the energies well outside of the CB range, even though it's not localized in energy to the CB, because of the non-local-in-energy character of $\text{Re}[\epsilon^{\text{eq}}(\omega)]$, as explained above.

We apply to the system a pump pulse of the form $\mathbf{A}_{\text{pu}}(t) = A_{\text{pu}}(t)\hat{\mathbf{j}}$ where $A(t)$ is given by

$$A_{\text{pu}}(t) = A_0 e^{-(4 \ln 2)t^2/\tau_{\text{pu}}^2} \cos(\omega_{\text{pu}} t), \quad (69)$$

in which, if not otherwise stated, the center of the pump pulse is taken as the origin of time, the FWHM of the pump pulse is $\tau_{\text{pu}} = 7\hbar/\Delta$, the frequency of the pump is $\omega_{\text{pu}} = 2.33\Delta/\hbar$, and the pump amplitude is $A_0 = 0.4\pi\hbar/ae$. The probe has the same polarization of the pump: $\lambda_{\text{pr}} = \hat{\mathbf{j}}$.

B. Peierls substitution coupling

At first, we consider (i) the system coupled to the pump pulse via the Peierls substitution and (ii) no dipole coupling between the VB and the CB. In Fig. 2, we present the transient behavior of the pumped system in such a case. Fig. 2(a) shows the transient differential absorption coefficient, as given by Eq. 46. The main red stripe in the VB and blue stripe in the CB coincide with the black-dashed lines that indicate the positions of the main peaks of the density of one-photon resonant states in each band, which is reported in panel (b). One should notice that at the resonances, the hole and electron populations mainly follow a Rabi-like behavior with a period much longer than the FWHM of the pump pulse, which results in the *accumulation* of the excitation populations. The electrons pumped into the CB leave less available states for the electrons to be excited by the probe pulse from the *core* band to the CB. Consequently, the absorption of the probe pulse is reduced that results in a blue stripe at the resonant energies of the CB. On the other hand, the photo-injected holes into the VB make it possible for the probe to excite electrons into the VB, which leads to a finite absorption and, hence, to the red stripe in the resonant energies of the VB. As we discussed in Ref. [49], the pump pulse is not single frequency, and, therefore, the resonance is not sharp and has a finite width, which explains the broadening of the main red and blue stripes around the resonance energies. Out of the resonance, the excitation population has some transient oscillations [49] with different amplitudes. The collective effects of all such oscillations in energy and time (as well as of the reso-

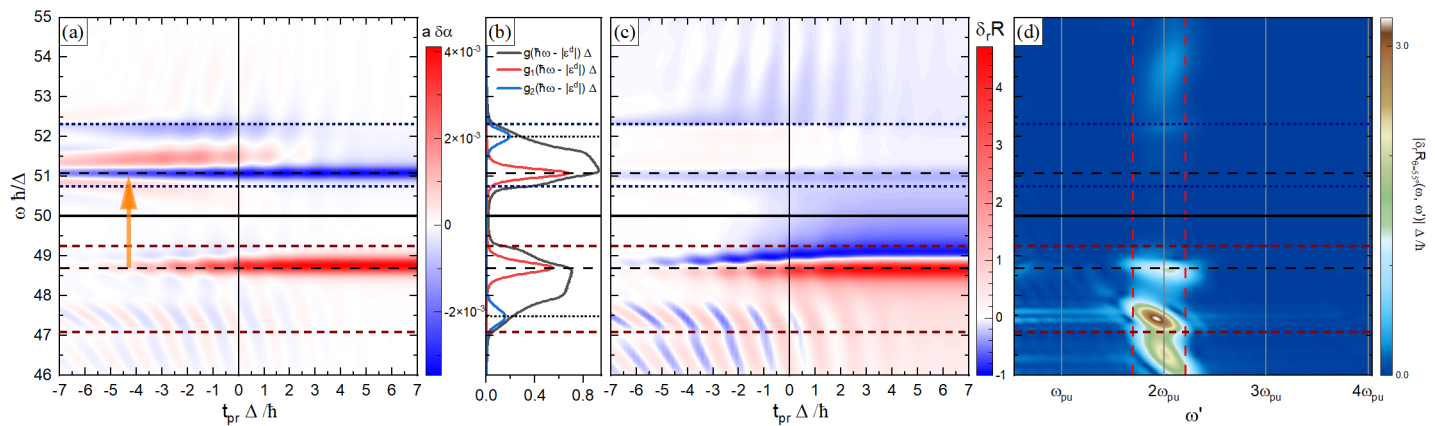


Figure 2. Transient optical behavior of the pumped system for the case of Peierls substitution coupling. (a) The transient differential absorption coefficient, as given by Eq. 46, vs probe time, t_{pr} , and probe photon frequency, ω . The orange arrow determines the main electronic excitation induced by the pump, which is the one-photon resonance. (b) DOS and the one- and two-photon DORS vs energy difference to the *core* band. (c) Transient relative differential reflectivity at the incident angle of $\theta = 55^\circ$, as defined in Eq. 43, vs delay time and probe photon energy. (d) The amplitude of the Fourier transformation of the transient reflectivity, $|\delta R_{\theta=55^\circ}(\omega, \omega')|$, see Eq. 44 (the low frequency region, $\omega' < 0.2\Delta/\hbar$, is not shown). The horizontal black-dashed lines indicate the peaks of the one-photon DORS, and the edges of VB (CB) are shown with dashed-wine (dotted-blue) lines.

nant ones) yield the other blue and red areas, as shown in the map, together with the modifications induced by the pump in the band structure of the system, to be intended as the time-dependent Hamiltonian matrix elements.

In Fig. 2(b), we show the density of states (DOS) and the one- and two-photon density of resonant states (DORS) vs energy, as given in the App. H. The peaks of the n_{ph} -photon DORS determine the energies at which one would expect the effects of resonances. Indeed, as we already discussed, the blue and red stripes in the map of $\delta\alpha$, in the CB and VB ranges, respectively, stem from the one-photon resonances. Notably, the two-photon resonances are very weak in this specific case and do not have any relevant effect on the scales of Fig. 2. This is mainly due to the peaks of the two-photon DORS being near the edges of the bands, where we have very small velocities and, hence, weak couplings to the pump pulse. This occurrence, together with the two-photon resonances being of second order and having low densities, results in a negligible role in the transient optical properties in this case.

In Fig. 2(c), we show the transient relative differential reflectivity at the incident angle $\theta = 55^\circ$, as defined in Eq. 43. In this map, we see that the peaks of the one-photon DORS (indicated by black-dashed lines) almost coincide with the narrow white regions, where $\delta_r R$ approaches zero. If one does not consider the imaginary part of the refraction index in the reflectivity calculation, they will coincide (not shown). This shows that the white narrow regions in the map of $\delta_r R$ indicate the absorption edges. Moreover, on this map, one can see the usual fishbone structure.

In Fig. 2(d), we show the amplitude of the Fourier transformation of the transient reflectivity,

$|\delta R_{\theta=55^\circ}(\omega, \omega')|$, as defined in Eq. 44. As it is clear from this map, the oscillatory part is around twice the pump frequency, $\omega' = 2\omega_{\text{pu}}$, and in particular, we don't have any odd-pump-frequency component. The absence of the odd-pump-frequency components in the system's response can be explained as follows. Writing the optical conductivity as the sum of the contributions from individual \mathbf{k} points, i.e., $\sigma(\omega, t_{\text{pr}}) = \sum_{\mathbf{k}} \sigma_{\mathbf{k}}(\omega, t_{\text{pr}})$, each single $\sigma_{\mathbf{k}}(\omega, t_{\text{pr}})$ can have odd-pump-frequency components that come from the coupling via the odd-terms in the expansion of the Peierls substitution which are proportional to the velocity and higher order odd derivatives (see Ref. [49]). Summing over all of the \mathbf{k} points on the grid these terms add up to zero because of the periodicity of the FBZ. This cancels out all odd-pump-frequency components in $\sigma(\omega, t_{\text{pr}})$, and consequently in the differential reflectivity.

C. Inter and intra-band transitions

In Fig. 3, we study the separate effects of the so-called inter- and intra-band transitions in the dynamics. To do that, one computes the projection coefficients, $P_{\mathbf{k}nn'}(t)$, from the Eq. 21, by considering just either the inter- or the intra-band transitions in the dynamics (see Ref. [49] for a detailed explanation). Fig. 3 (top-left panel) shows the transient differential absorption coefficient with only the inter-band transitions active. In this case, the energies where we have one-photon resonances (the one-photon-resonance energies) are even more relevant than in the case of full dynamics (Fig. 2(a)), as the off-resonance energies become less relevant without the intra-band transitions.

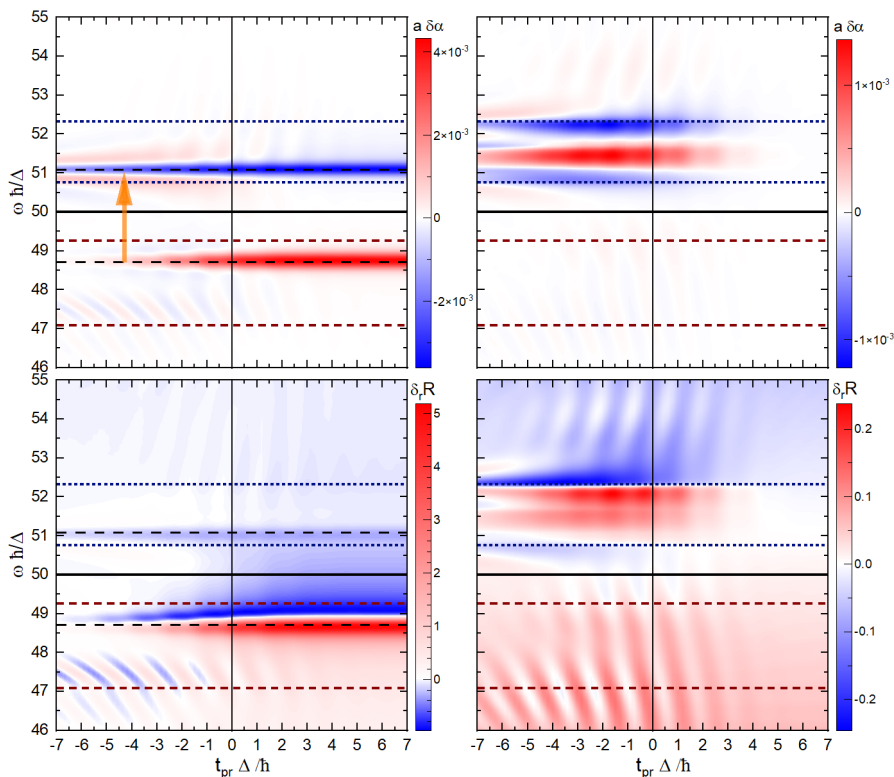


Figure 3. Transient (top row) differential absorption and (bottom row) relative differential reflectivity, with (left column) only inter-band and (right column) only intra-band transitions in the dynamics, vs delay time and probe photon energy. The horizontal lines are the same as those of Fig. 2.

Fig. 3 (top-right panel) shows the transient differential absorption coefficient with only the intra-band transitions active. In this case, the resonant energy gaps are no longer relevant because there is no electron transition among the bands, so the resonance loses meaning. Given that with our system and pump parameters, the resonance effects are the most relevant ones (see Fig. 2(a)), this may lead to the conclusion that the intra-band motion is irrelevant. The qualitative shape of the color map, i.e., the photon energies at which positive or negative (red or blue, respectively) signals appear, is almost independent of the pump frequency (see Fig. 11 in App. I), even though the details of the oscillations depend on it. Consequently, the main features for this case are determined by the electronic bands and their couplings to the pump pulse (i.e., to the system properties) rather than to the pump-pulse parameters. A comparison between the full-dynamics case and the cases for only inter- and intra-band transitions active reveals that each type of transition contributes with specific features, but that only the interplay between them can explain the full-dynamics case. The features caused by inter-band transitions are the dominant ones. The lower relevance of intra-band transitions is due to the smoothness of the bands caused by the short range and the relatively small values of the hoppings. This leads to relatively small changes in the bands upon shifting the momentum by the vector poten-

tial through the Peierls substitution.

In Fig. 3 (bottom-left/bottom-right panel), we have the transient relative differential reflectivity for the case of having only inter-/intra-band transitions in the dynamics. Similar to the case of absorption, we see that there are features in the full-dynamics case originating from either of the inter- or intra-band transitions and the interplay of the two types of transitions results in the full picture (compare with Fig. 2(c)).

D. Dipole coupling

Now, we study the effect of having a finite local dipole, in addition to the Peierls substitution coupling. Let us consider local dipole elements $\hat{\mathbf{D}}_{\mathbf{R}=0,1,2} = \hat{\mathbf{D}}_{\mathbf{R}=0,2,1}^* = i0.05a\hat{\mathbf{j}}$. In Fig. 4 (top-left panel), we show the transient differential absorption coefficient for such a case. Similar to the former case, the main change in the absorption occurs at the one-photon resonance energies in the VB and CB. In this case, the changes in the absorption are higher as the local dipole strengthens the excitation rates of electrons from the VB to CB.

In Fig. 4 (middle panel), we show the transient relative differential reflectivity at the incident angle $\theta = 55^\circ$, $\delta R_{\theta=55^\circ}(\omega, t_{\text{pr}})$. We see that the *white lines* that determine the absorption edges are somewhat distorted under

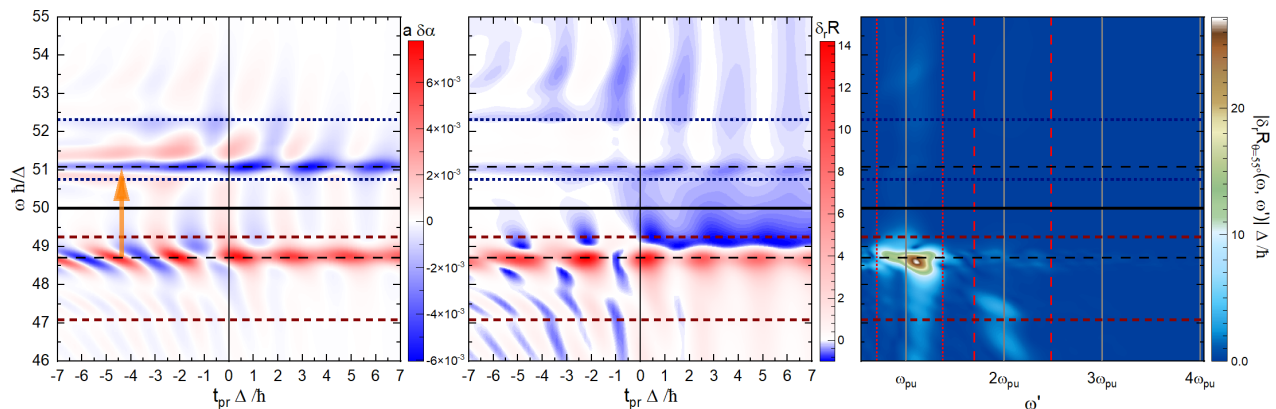


Figure 4. Transient optical behavior of the pumped system with both the local dipole and the Peierls substitution coupling with the pump. (left) The transient differential absorption coefficient, as given by Eq. 46, and, (middle) transient relative differential reflectivity at the incident angle of $\theta = 55^\circ$, vs delay time and probe photon energy. (right) The amplitude of the Fourier transformation of the transient reflectivity, $|\delta R_{\theta=55^\circ}(\omega, \omega')|$, see Eq. 44 (we don't show the low frequency region, $\omega' < 0.2\Delta/\hbar$). The horizontal lines are the same as those of Fig. 2.

the effect of the local dipole coupling. This is due to the off-resonant non-permanent-excitation oscillations at other energies that are strengthened by the local dipole and can have more long-range tails in energy.

Comparison between Figs. 2 and 4 clarifies that the oscillations are different in the two cases. This can be well understood from Fig. 4 (right panel), where we show the amplitude of the Fourier transformation of the transient reflectivity, $|\delta R_{\theta=55^\circ}(\omega, \omega')|$. The main difference with the former case is that here we do have the odd-pump-frequency components, and in particular, ω' around $1\omega_{pu}$ giving the most substantial contribution in the oscillatory behavior. The odd-pump-frequency components come from the coupling to the pump-pulse electric field via the local dipole. Such contributions are not canceled upon the summation over the entire k grid, unlike what happens for the velocity and higher-order odd-derivatives in the Peierls substitution, and instead significantly contribute to the system's response.

Such odd-pump-frequency components did not show up in our recent work on germanium [38], which indicates that the effects of local dipole moments between the VB and CB were negligible there (even though the dipole between the core levels and the VB/CB is noticeable), as was further confirmed by our DFT calculations. Moreover, in many other materials, the odd-pump-frequency components are negligible, which justifies ignoring the local dipole coupling and keeping only the Peierls substitution, as it is done by some authors (see Ref. [50] and the references therein). Given these results, we consider zero dipole coupling between the VB and CB in the following calculations and keep only the Peierls substitution. Another point that is worthy of being mentioned is that the $2\omega_{pu}$ -component is different from the case of having no local dipole, Fig. 2. It shows the interplay between the two terms, which clarifies that one cannot consider their effects irrespective of each other.

E. Pump-pulse frequency dependence

In Fig. 5, we study the effect of changing the pump-pulse frequency to better understand the role of resonances with the pump-pulse frequency in the out-of-equilibrium optical properties. The FWHM of the pump pulse, τ_{pu} , is also changed in such a way that, in all three cases, $\omega_{pu}\tau_{pu}$ remains the same as the one of Fig. 2. In Fig. 5 (top-left panel), we show the transient differential absorption coefficient for the case of $\hbar\omega_{pu}/\Delta = 1$. It is worth noting that the minimum gap energy in our system, which is at Γ , is 1.5Δ , which is higher than $\hbar\omega_{pu}$, and therefore we have no one-photon resonances. However, this map indicates a main absorption process at the two-photon resonant k -points (a green arrow indicates the two-photon transitions) at the energies where we have the peaks of the two-photon DORS, as indicated by the black-dotted lines. The process is of the second order; hence, the absorption change is lower than in the former cases. The bottom-left panel shows the transient relative differential reflectivity for the same pump-pulse parameters. Again, the peaks of the two-photon DORS (signaled by black-dotted lines) indicate the absorption edges, though they are not as intense as the first-order transitions.

In Fig. 5 (top-middle and bottom-middle panels), we show the transient differential absorption coefficient and relative differential reflectivity, respectively, for $\hbar\omega_{pu}/\Delta = 1.5$. The pump-pulse frequency resonates with the minimum energy gap at Γ . Therefore, the upper/lower edges of the VB/CB determine the one-photon-resonance energies and almost coincide with the peaks of the one-photon DORS and, consequently, the main absorption stripes. In addition to the one-photon resonances, we also see the effects of the two-photon resonances, which are of the second order (the peaks of the two-photon DORS are signaled by black-dotted lines, and

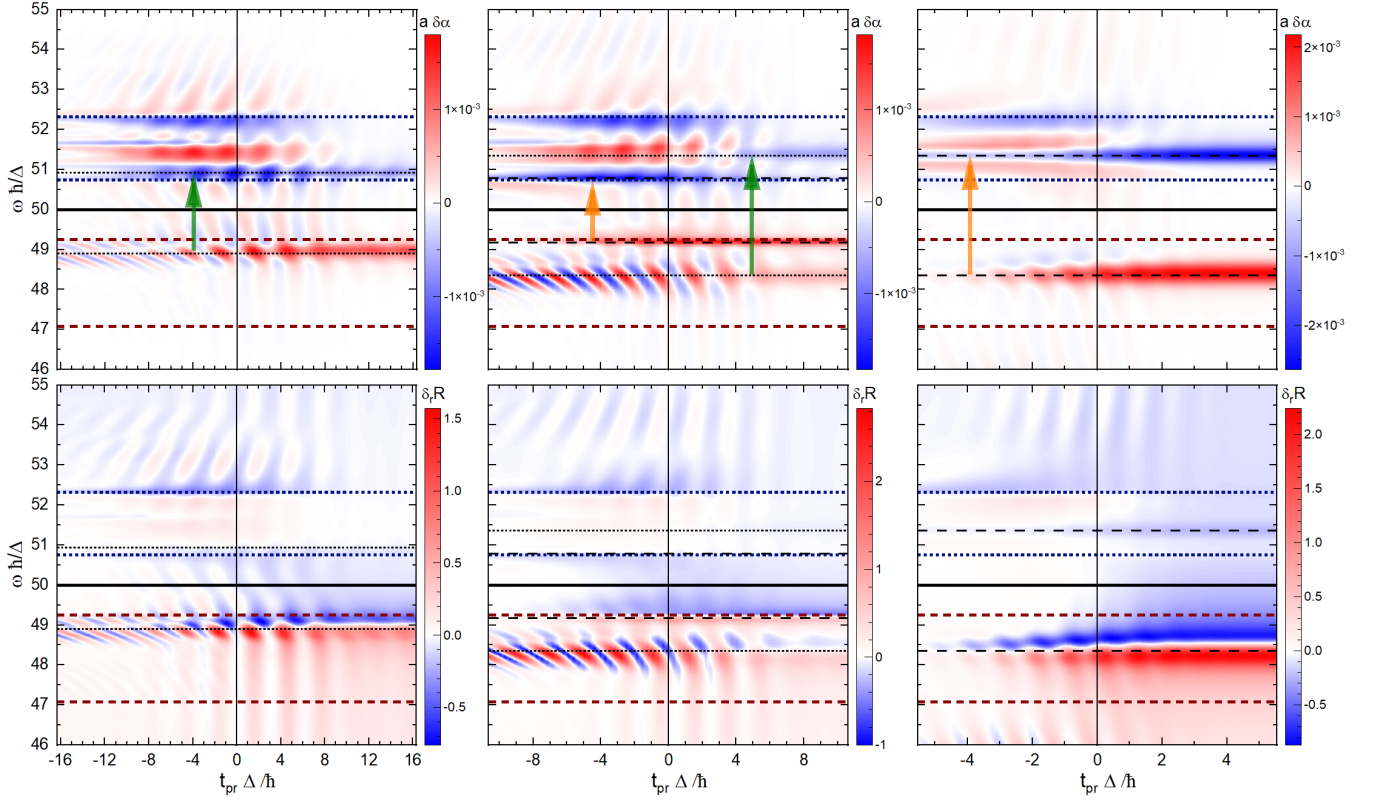


Figure 5. (top row) Transient differential absorption coefficients and (bottom row) transient relative differential reflectivities, vs delay time and probe photon energy, for three different pump-pulse frequencies: (left column) $\hbar\omega_{\text{pu}}/\Delta = 1$, (middle column) $\hbar\omega_{\text{pu}}/\Delta = 1.5$ and (right column) $\hbar\omega_{\text{pu}}/\Delta = 3$. For each ω_{pu} , the FWHM of the pump pulse, τ_{pu} , is set in such a way that $\omega_{\text{pu}}\tau_{\text{pu}}$ remains the same as the one of Fig. 2. The orange (green) arrows indicate the one-photon (two-photon) transitions, if any, while the horizontal black-dashed (-dotted) lines determine the peaks of one-photon (two-photon) DORS, if any.

and a green arrow indicates the two-photon transitions). Both first-order and second-order transitions result in their corresponding absorption edges in the transient relative differential reflectivity, with the difference that the absorption edges of the two-photon resonances are less intense than the ones of the one-photon resonances.

In Fig. 5 (top-right and bottom-right panels), we show the transient differential absorption coefficient and relative differential reflectivity, respectively, for $\hbar\omega_{\text{pu}}/\Delta = 3$. In this case, we have only the one-photon resonances, with their corresponding effects in the absorption and reflectivity, similar to the ones of Fig. 2. It is noteworthy that in this case, because of the high value of ω_{pu} , we don't have two-photon resonances at all. On the other hand, in the case of Fig. 2, even though we do have two-photon resonances, they have much smaller effects than the one-photon ones because they occur near the edges of the VB and CB and, hence, (i) they are coupled very weakly to the pump pulse (their velocity is small) and (ii) they have a smaller DORS than the one-photon resonances (see also Ref. [49]).

F. Pump-pulse intensity dependence

Another relevant study investigates the effect of the pump-pulse intensity. The complete maps with different intensities look qualitatively similar (not shown), and for a better understanding, we look at some specific probe frequencies. For this purpose, we considered two probe frequencies in Fig. 6: $\hbar\omega/\Delta = 48.72$ and 51.07 . In the top panels of Fig. 6, we consider three different pump-pulse intensities: $0.5I_0$, I_0 and $2I_0$, where I_0 corresponds to the pump-pulse intensity of Fig. 2 (other parameters are also the same as the ones of Fig. 2), and plot the transient differential absorption coefficients, and the transient relative differential reflectivities, vs. the probe time. At each instant of time, one cannot find a power-law behavior for either of the quantities. Nevertheless, the order is respected; generally speaking, increasing the intensity increases the strength of the signals.

In the bottom panels of Fig. 6, we plot the absolute value of the residual differential absorption coefficient, $|\delta\alpha(\omega, t_{\text{pr}} \rightarrow +\infty)|$, and the absolute value of the residual relative differential reflectivity, $|\delta R_{\theta=55^\circ}(\omega, t_{\text{pr}} \rightarrow +\infty)|$, vs. the pump-pulse intensity (note that $t_{\text{pr}} \rightarrow +\infty$ means

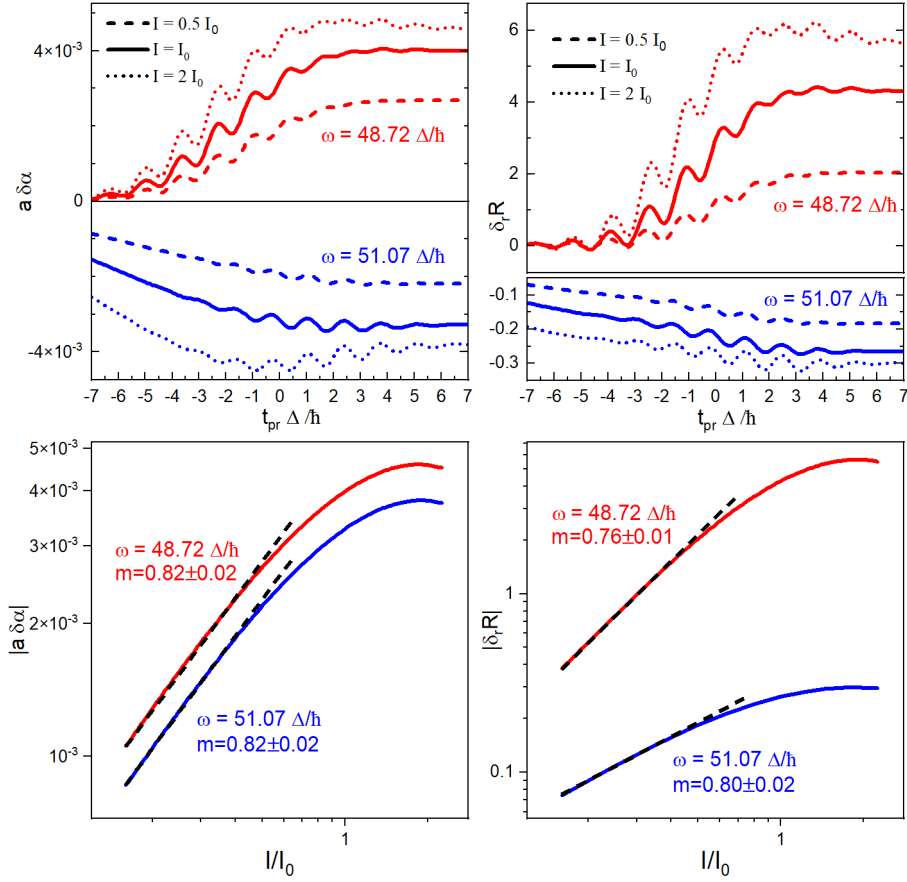


Figure 6. Study of the intensity dependence, for two probe frequencies: $\hbar\omega/\Delta = 48.72$ and 51.07 . (top-left) The transient differential absorption coefficient, and (top-right) the transient relative differential reflectivities, vs the probe time, for three different pump-pulse intensities: $0.5I_0$, I_0 and $2I_0$, where I_0 corresponds to the pump-pulse intensity of Fig. 2 (other parameters are also the same as the ones of Fig. 2). The absolute values of, (bottom-left) the residual differential absorption coefficient, and (bottom-right) the residual relative differential reflectivity, vs the pump-pulse intensity. The slope of each curve, m , is written next to it.

a time well after the application of the pump pulse, but still much smaller than the time scale of the other decoherence and de-excitation transitions, such as electron-phonon interaction, spontaneous emission, etc.). We see a linear behavior in the logarithmic plot for lower intensities, which means a power-law dependence on the intensity. The slope of the logarithmic plot, m , is the power of the dependence and, in our cases, is always below 1. The one-photon resonance is the main process in our model for $\omega_{pu} = 2.33\Delta/\hbar$. But the power is less than 1, as all orders of the Peierls expansion co-exist and affect each other (see Refs. [38] and [49] for more discussion). For higher intensities, the curves bend and show no more a power-law behavior. This can be explained by noting that the excitations are far below the population inversion for low intensities, and by varying the intensity, one can find a power law. Increasing the intensity increases the Rabi frequency, which results in excitations closer to the full population inversion. Hence, we do not find a power law behavior with respect to the intensity anymore.

G. IR and visible regime

Up to now, we have been studying the probes in the high-frequency regime of XUV. Now, we move to probes in the low-frequency regime, which corresponds to IR and visible regimes, which we denote by IR-V. Based on our arguments in App. B, using the standard formulas for the transient optical properties (reflectivity and absorption) in this regime is not straightforward. Indeed, to study the transient optical behavior, we can safely investigate the transient differential imaginary and real parts of the dielectric function (see also App. G).

In Fig. 7 (left panel), we show the imaginary and real parts of the dielectric function at equilibrium in the IR-V regime. In this regime, we use $0^+ = 0.1\Delta/\hbar$ (see App. F, Fig. 9). The *core* bands play no role, and the probe pulse induces transitions between the VB and CB. The green-dotted lines determine the minimum and maximum values of the gap energies and the CB-VB gap, $\varepsilon_{\mathbf{k}}^c - \varepsilon_{\mathbf{k}}^v$, along the main path in the \mathbf{k} space is shown in the inset. $\text{Re}[\varepsilon^{\text{eq}}(\omega)]$ decreases outside of the energy range of the

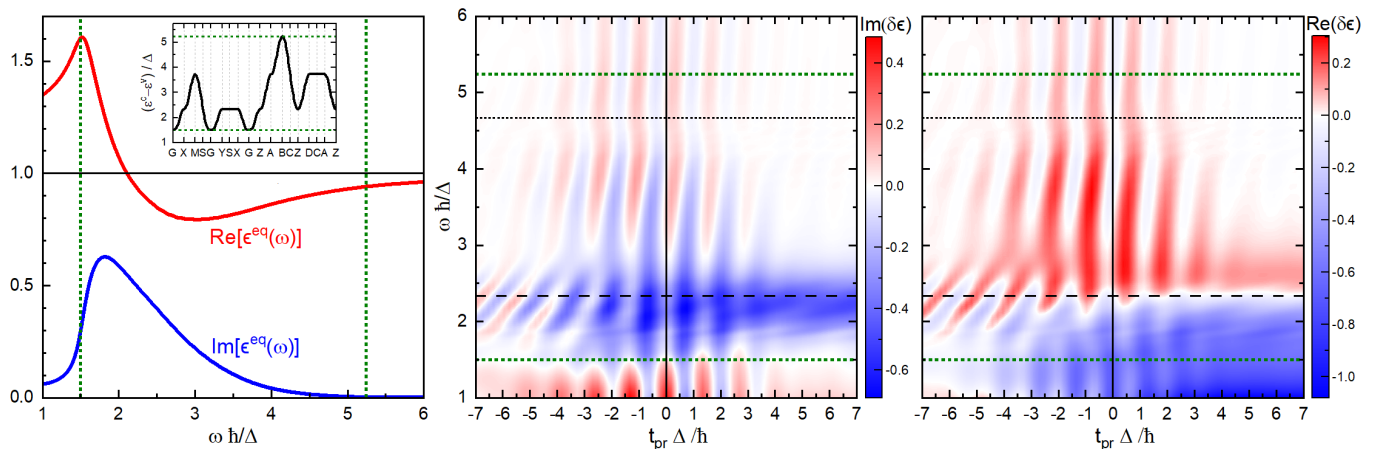


Figure 7. Optical properties in the IR-V regime. (left) The imaginary and real parts of the dielectric function at equilibrium. The inset shows the gap, $\varepsilon_{\mathbf{k}}^c - \varepsilon_{\mathbf{k}}^v$, along the main path in the \mathbf{k} space. The transient differential (middle) imaginary and (right) real parts of the dielectric function. The green-dotted lines determine the minimum and maximum values of the gap energies and the black-dashed (-dotted) line show the energy of one-(two)-photon resonance.

gap energies and tends to its predicted value for $\omega \rightarrow 0$ (see Eq. 51). The $\text{Im}[\varepsilon^{\text{eq}}(\omega)]$ is finite only in the range of the gap energies, but because of the finite value of 0^+ , it doesn't tend to zero for $\omega \rightarrow 0$. Instead, as shown in Eq. 51, it artificially diverges in this limit (not shown).

Fig. 7 (middle panel) shows the imaginary part of the transient differential dielectric function. At the pump-pulse frequency, we have the most relevant resonant excitation process. The electrons get excited from the VB to CB, reducing the absorption of the probe-pulse via the same process, as there remain fewer available electrons in the VB and vacancies in the CB, hence, a bright blue stripe. In the right panel of Fig. 7, we report the real part of the transient differential dielectric function, which shows a clear absorption edge at the resonance energy. It is noteworthy that, as we mentioned before, the two-photon resonance is very weak in this case; hence, there is almost no signature at its corresponding energy.

IV. SUMMARY

We provided the linear response theory to a weak probe pulse for a pumped system out of equilibrium. Such a theory speeds up numerical calculations enormously, as one needs to simulate the pumped system only once instead of considering the probe repeatedly for all pump-probe delays.

Applying this theory to a generic semiconductor system with a quadratic Hamiltonian in the dipole gauge and using the recently developed theory, Dynamical Projective Operatorial Approach, we derive a formula for computing the optical conductivity as a function of the pump-probe delay time and the probe photon frequency, from which one can obtain the transient reflectivity and absorption. We provided several essential guidelines that would make it possible to perform actual numerical cal-

culations with affordable computational costs.

By considering a prototypical three-band (valence, conduction, and core) model system, which is pumped in the frequency range that can excite electrons between valence and conduction bands (which is assumed to be the IR range), we computed transient optical properties in the probe photon frequency range of the gaps between the core band and the other bands (which is assumed to be the XUV range). We provided a systematic way to analyze such results to find the relation between the features in the transient differential absorption and reflectivity and the system band structure in the first Brillouin zone. We also proposed and exploited some generalizations of the density of states related solely to the resonant states. Moreover, we studied the effect of a local dipole and different mechanisms, such as inter-band and intra-band transitions and single- and multi-photon processes. The latter is further analyzed by changing the photon frequency to explore various regions of the first Brillouin zone in terms of being in resonance with the pump pulse. Furthermore, we studied the effect of the pump pulse intensity. Finally, we investigated the transient optical response for the IR and visible range and analyzed the results and their relations to the system and pump pulse features.

Our work is at least of two-fold relevance: (i) we provide a theoretical method that can be affordably applied to simulate realistic experimental setups, and (ii) we give a systematic way to analyze the results of optical measurements in terms of the system properties and pump pulse parameters.

ACKNOWLEDGMENTS

The authors thank Claudio Giannetti, Matteo Lucchini, Stefano Pittalis, and Carlo Andrea Rozzi for the

insightful discussions. The authors acknowledge support by MIUR under Project No. PRIN 2017RKWTMY.

Appendix A: The linear variation of the density matrix in the presence of the probe pulse

The time evolution of the density matrix of the pumped system, $\hat{\Upsilon}'(t)$, is given by the following equation of motion

$$i\hbar \frac{\partial}{\partial t} \hat{\Upsilon}'(t) = \left[\hat{H}'(t), \hat{\Upsilon}'(t) \right], \quad (\text{A1})$$

with generalized solution

$$\hat{\Upsilon}'(t) = \hat{U}'(t, t_{\text{ini}}) \hat{\Upsilon}_0 \hat{U}'(t_{\text{ini}}, t), \quad (\text{A2})$$

where $\hat{\Upsilon}_0$ is the density matrix at the time $t_{\text{ini}} \rightarrow -\infty$ (i.e., at a time preceding the application of the pump) and,

$$\hat{U}'(t_1, t_2) = T_+ \left[e^{-\frac{i}{\hbar} \int_{t_2}^{t_1} dt' \hat{H}'(t')} \right], \quad (\text{A3})$$

is the time propagator in which T_+ is the time-ordering operator.

The full density matrix of the system in the presence of both the pump and probe pulses, $\hat{\Upsilon}(t)$, obeys the following equation of motion,

$$i\hbar \frac{\partial}{\partial t} \hat{\Upsilon}(t) = \left[H(t), \hat{\Upsilon}(t) \right]. \quad (\text{A4})$$

We need to consider the full effect of the pumping via $\hat{H}'(t)$, but consider the effect of the probe pulse up to the linear order in $\hat{H}''(t)$. In order to do that, we move to an interaction picture in which the Hamiltonian of the probe pulse, $\hat{H}''(t)$, is considered as the interaction term. The operators in this picture are indicated by the subscript \hat{H}' and given by Eq. 3. The full density matrix in this picture is given by,

$$\hat{\Upsilon}_{H'}(t) = \hat{U}'(t_{\text{ini}}, t) \hat{\Upsilon}(t) \hat{U}'(t, t_{\text{ini}}). \quad (\text{A5})$$

It is straightforward to perform a direct time derivation and show that $\hat{\Upsilon}_{H'}(t)$ obeys the following equation of motion,

$$i\hbar \frac{\partial}{\partial t} \hat{\Upsilon}_{H'}(t) = \left[\hat{H}_{H'}''(t), \hat{\Upsilon}_{H'}(t) \right], \quad (\text{A6})$$

with generalized solution

$$\hat{\Upsilon}_{H'}(t) = \hat{U}''(t, t_{\text{ini}}) \hat{\Upsilon}_0 \hat{U}''(t_{\text{ini}}, t), \quad (\text{A7})$$

where

$$\hat{U}''(t_1, t_2) = T_+ \left[e^{-\frac{i}{\hbar} \int_{t_2}^{t_1} dt' \hat{H}_{H'}''(t')} \right]. \quad (\text{A8})$$

Combining Eqs. A2, A5 and A7, the probe-pulse-induced variation of the density matrix is obtained as,

$$\hat{\Upsilon}(t) - \hat{\Upsilon}'(t) = \hat{U}'(t, t_{\text{ini}}) \left(\hat{\Upsilon}_{H'}(t) - \hat{\Upsilon}_0 \right) \hat{U}'(t_{\text{ini}}, t). \quad (\text{A9})$$

Up to the linear order in $\hat{H}''(t)$, we have

$$\hat{U}''(t_1, t_2) \simeq 1 - \frac{i}{\hbar} \int_{t_2}^{t_1} dt' \hat{H}_{H'}''(t'). \quad (\text{A10})$$

Substituting Eq. A10 in Eq. A7 and then in Eq. A9, we obtain the linear order variation of the density matrix, as given in Eq. 4 in the main text.

Appendix B: Dielectric function and the reflectivity formula out of equilibrium

1. Dielectric function

In order to obtain the dielectric function from the conductivity out of equilibrium, we recall that the continuity equation for \mathbf{j}_{pr} , the electrical current induced by the probe pulse, reads as

$$\nabla \cdot \mathbf{j}_{\text{pr}}(t) + \partial_t \rho_{\text{pr}}(t) = 0, \quad (\text{B1})$$

where $\rho_{\text{pr}}(t)$ is the bounded charge density induced only by the probe pulse, and for the sake of simplicity, we showed only the time dependence explicitly. The probe pulse induced quantities (such as current, charge density, etc.) are obtained as the difference between the value of the quantities in the presence of both pump and probe pulses and their value in the presence of the pump pulse only.

The bounded charge density satisfies the Gauss's law, as

$$\nabla \cdot [\epsilon_0 \mathbf{E}_{\text{pr}}(t) - \mathcal{D}_{\text{pr}}(t)] = \rho_{\text{pr}}(t), \quad (\text{B2})$$

where $\mathcal{D}_{\text{pr}}(t)$ is the electric displacement field of the probe pulse, i.e., it is constructed from the electric field of the probe pulse and the probe-pulse induced charge polarization. Combining Eqs. B1 and B2 and considering the boundary conditions, we arrive at the following formula,

$$\mathbf{j}_{\text{pr}}(t) + \epsilon_0 \partial_t \mathbf{E}_{\text{pr}}(t) - \partial_t \mathcal{D}_{\text{pr}}(t) = 0. \quad (\text{B3})$$

The responses to the probe pulse are assumed to be linear, so that one can write

$$\mathbf{j}_{\text{pr}}(t) = \int dt' \boldsymbol{\sigma}(t, t') \cdot \mathbf{E}_{\text{pr}}(t'), \quad (\text{B4})$$

and

$$\mathcal{D}_{\text{pr}}(t) = \epsilon_0 \int dt' \boldsymbol{\epsilon}(t, t') \cdot \mathbf{E}_{\text{pr}}(t'), \quad (\text{B5})$$

where $\epsilon(t, t')$ is the (dimensionless) dielectric function of the material and ϵ_0 is the vacuum permeability. Substituting back in Eq. B3, performing a Fourier transformation with respect to the time $(t - t')$, and using integration by parts to deal with the time derivatives, we get

$$\int dt' \epsilon(\omega, t') \cdot e^{i\omega t'} \mathbf{E}_{\text{pr}}(t') = \int dt' e^{i\omega t'} \mathbf{E}_{\text{pr}}(t') + \frac{i}{\omega \epsilon_0} \int dt' \boldsymbol{\sigma}(\omega, t') \cdot e^{i\omega t'} \mathbf{E}_{\text{pr}}(t'). \quad (\text{B6})$$

Note that the response functions $\boldsymbol{\sigma}(\omega, t')$ and $\epsilon(\omega, t')$ depend only on the material and the pump pulse, and the above equation should hold for any probe pulse, $\mathbf{E}_{\text{pr}}(t')$. Consequently, one can eliminate $\int dt' e^{i\omega t'} \mathbf{E}_{\text{pr}}(t')$ and arrive at the following relation which computes the dielectric function from the conductivity:

$$\epsilon(\omega, t) = \mathbf{1} + \frac{i}{\omega \epsilon_0} \boldsymbol{\sigma}(\omega, t). \quad (\text{B7})$$

2. Reflectivity

Starting from the Maxwell's equations, after some straightforward algebra and using Eq. B5 we obtain

$$\nabla^2 \mathbf{E}_{\text{pr}}(\omega) = -\mu_0 \epsilon_0 \omega^2 \int dt' e^{i\omega t'} \epsilon(\omega, t') \cdot \mathbf{E}_{\text{pr}}(t'), \quad (\text{B8})$$

and

$$\nabla^2 \mathbf{B}_{\text{pr}}(\omega) = -i\mu_0 \epsilon_0 \omega \int dt' e^{i\omega t'} \epsilon(\omega, t') \cdot \partial_{t'} \mathbf{B}_{\text{pr}}(t'), \quad (\text{B9})$$

where \mathbf{B}_{pr} is the magnetic field of the probe pulse and we have considered a non-magnetic material, so that the magnetic susceptibility of the material is just the one of vacuum, μ_0 .

To proceed further, we need to apply some approximations. It is noticeable that for the majority of the experimental setups, performing a Fourier transformation of $\epsilon(\omega, t')$ with respect to t' , the highest frequency content would be around $n\omega_{\text{pu}}$, with usually at most $n \approx 2$. If the width of the probe envelope is much less than the oscillation period of the pump pulse, one can approximately take $\epsilon(\omega, t')$ out of the above integrals. Given that the probe pulse oscillation period should be smaller than the width of its envelope, our approximation holds only when the probe pulse frequency is much higher than the one of the pump pulse. Under such circumstances, one can write:

$$\nabla^2 \mathbf{E}_{\text{pr}}(\omega) = -\mu_0 \epsilon_0 \omega^2 \epsilon(\omega, t_{\text{pr}}) \cdot \mathbf{E}_{\text{pr}}(\omega), \quad (\text{B10})$$

and

$$\nabla^2 \mathbf{B}_{\text{pr}}(\omega) = -\mu_0 \epsilon_0 \omega^2 \epsilon(\omega, t_{\text{pr}}) \cdot \mathbf{B}_{\text{pr}}(\omega), \quad (\text{B11})$$

where t_{pr} is the center of the probe pulse and the integration by parts has been used in the equation for the magnetic field.

Eqs. B10 and B11 ensure that, under the approximations we have considered, the probe pulse behaves similarly to the equilibrium case with the dielectric function given by $\epsilon(\omega, t_{\text{pr}})$. Consequently, one can apply the same procedure as at equilibrium and obtain the formula for reflectivity given in Eq. 42.

Appendix C: Considering only the transitions from the core levels in optical conductivity

It is possible to assume that the high-frequency XUV probes detect only the gaps between core bands and those bands near the Fermi energy (either valence or conduction, which we call *surface* bands, and indicate by n_s). This approximation works better for larger core-surface energy gaps. After some straightforward calculations, one can show that the optical conductivity within this approximation becomes

$$\begin{aligned} \sigma(t, t_{\text{pr}}) &\approx \frac{e}{\hbar \mathcal{V}} \theta(t - t_{\text{pr}}) \\ &\sum_{\mathbf{k}} \int_{t_{\text{pr}}}^t dt' \sum_{n_s n'_s n''_s n_{\text{core}}} \text{Im} [\mathbf{J}_{\mathbf{k}}^{n_s n_{\text{core}}}(t) \\ &\left(-\frac{e}{\hbar} \mathbf{V}_{\mathbf{k}}^{n_{\text{core}} n'_s}(t') + e \mathbf{D}_{\mathbf{k}}^{n_{\text{core}} n'_s}(t_{\text{pr}}) \delta(t' - t_{\text{pr}}) \right) \\ &e^{-i\omega_{\mathbf{k} n_{\text{core}}}(t-t')} P_{\mathbf{k} n_s n''_s}^*(t) P_{\mathbf{k} n'_s n''_s}(t') (1 - f_{\mathbf{k} n''_s}) \Big]. \quad (\text{C1}) \end{aligned}$$

Unfortunately, the equilibrium conductivity computed via this approximation has a non vanishing $1/(\omega + i0^+)$ tail. This can be understood from Eq. 50 as it has no core-surface term, unlike Eq. 49. For the cases like our toy-model this doesn't bring any problem, and the results of this approximation are almost exactly the same as the ones obtained from the full formula. However, in realistic situations this approximation may fail, not only because of the non-vanishing tail, but also for the effects of surface-surface transitions even on the conductivity in XUV frequency range.

Appendix D: Cancellation of the equilibrium tails at zero temperature

We consider only the diagonal elements of the optical conductivity. Accordingly, we use $\sigma = \boldsymbol{\lambda} \cdot \boldsymbol{\sigma} \cdot \boldsymbol{\lambda}$ where $\boldsymbol{\lambda}$ is the unit vector of a generic direction. The diagonal second tail term in equilibrium, Eq. 50, can be rewritten as

Appendix E: Quasi-static approximation

$$\sigma_2^{\text{eq,tail}}(\omega) = \frac{ie^2}{\hbar^2\mathcal{V}(\omega+i0^+)} \sum_{\mathbf{k}n} f_{\mathbf{k}n} \sum_{\nu_1\nu_2} \Omega_{\mathbf{k}\nu_1 n}^* \left[\partial_{k_{\parallel}}^2 \tilde{T}_{\mathbf{k}}^{\nu_1\nu_2} \right] \Omega_{\mathbf{k}\nu_2 n}, \quad (\text{D1})$$

where $k_{\parallel} = \boldsymbol{\lambda} \cdot \mathbf{k}$. Here we consider a fully gapped system (e.g., a semiconductor) at zero temperature, so that $f_{\mathbf{k}n}$ doesn't depend on \mathbf{k} , but it is just a function of n , and can be only 1 or 0. As such, $\partial_{k_{\parallel}} f_{\mathbf{k}n} = 0$, and one can use the periodicity of the FBZ to perform an integration by part and write $\sigma_2^{\text{eq,tail}}(\omega)$ as,

$$\sigma_2^{\text{eq,tail}}(\omega) = -\frac{ie^2}{\hbar^2\mathcal{V}(\omega+i0^+)} \sum_{\mathbf{k}n} f_{\mathbf{k}n} \left\{ \left[\partial_{k_{\parallel}} \Omega_{\mathbf{k}}^{\dagger} \right] \Omega_{\mathbf{k}} \eta_{\mathbf{k}} + \eta_{\mathbf{k}} \Omega_{\mathbf{k}}^{\dagger} \left[\partial_{k_{\parallel}} \Omega_{\mathbf{k}} \right] \right\}_{nn} \quad (\text{D2})$$

where, for the sake of simplicity, a compact matrix notation has been used, $\{M\}_{nn'}$ is the nn' element of matrix M , and $\eta_{\mathbf{k}} = \boldsymbol{\lambda} \cdot \boldsymbol{\eta}_{\mathbf{k}} = \Omega_{\mathbf{k}}^{\dagger} \left[\partial_{k_{\parallel}} \tilde{T}_{\mathbf{k}} \right] \Omega_{\mathbf{k}}$. Then, we exploit the following relation [51],

$$\left\{ \Omega_{\mathbf{k}}^{\dagger} \left[\partial_{k_{\parallel}} \Omega_{\mathbf{k}} \right] \right\}_{nn'} = \begin{cases} -\frac{\eta_{\mathbf{k}}^{nn'}}{\hbar\omega_{\mathbf{k}nn'}} & n \neq n', \\ 0 & n = n', \end{cases} \quad (\text{D3})$$

to obtain

$$\sigma_2^{\text{eq,tail}}(\omega) = -\frac{ie^2}{\hbar^3\mathcal{V}(\omega+i0^+)} \sum_{\mathbf{k}n} f_{\mathbf{k}n} \sum_{n' \neq n} \left(\frac{\eta_{\mathbf{k}}^{nn'} \eta_{\mathbf{k}}^{n'n}}{\omega_{\mathbf{k}nn'}} - \frac{\eta_{\mathbf{k}}^{nn'} \eta_{\mathbf{k}}^{n'n}}{\omega_{\mathbf{k}n'n}} \right), \quad (\text{D4})$$

which after some straightforward calculations can be rewritten as

$$\sigma_2^{\text{eq,tail}}(\omega) = \frac{ie^2}{\hbar^3\mathcal{V}(\omega+i0^+)} \sum_{\mathbf{k}nn'} \frac{\eta_{\mathbf{k}}^{nn'} \eta_{\mathbf{k}}^{n'n} (f_{\mathbf{k}n'} - f_{\mathbf{k}n})}{\omega_{\mathbf{k}nn'}}. \quad (\text{D5})$$

Comparing Eqs. 49 and D5, one verifies that

$$\sigma_1^{\text{eq,tail}}(\omega) + \sigma_2^{\text{eq,tail}}(\omega) = 0. \quad (\text{D6})$$

A crucial point in this proof is that the distribution function, $f_{\mathbf{k}n}$, is independent of \mathbf{k} . This is clearly the case for fully gapped systems at zero temperature, where indeed we have no DC conductivity and the tails should cancel each other which results in a vanishing Drude weight [50]. On the other hand, if the temperature is not zero or the system is metallic (non-gapped), this condition breaks down and we can have DC conductivity as the tail terms don't cancel each other.

One approximation is to assume that the probe frequency is much higher than the one of the pump pulse, so that one can consider the system to be quasi static in the vicinity of the probing time t_{pr} . For such an approximation, one computes the dynamics up to t_{pr} according to Eq. 21 to obtain $P_{\mathbf{k}}(t_{\text{pr}})$, but, for those times larger than t_{pr} , one considers the Hamiltonian as time independent. Diagonalizing $H'_{\mathbf{k}}(t_{\text{pr}})$ using a unitary matrix $U_{\mathbf{k}}(t_{\text{pr}})$, one can simply show that the quasi-static projection coefficients in this diagonal basis, $P_{\mathbf{k}ln}^{\text{qs}}(t)$, are given by

$$P_{\mathbf{k}ln}^{\text{qs}}(t) = e^{-i(t-t_{\text{pr}})\omega_{\mathbf{k}l}(t_{\text{pr}})} P_{\mathbf{k}ln}^{\text{qs}}(t_{\text{pr}}) \quad t \geq t_{\text{pr}} \quad (\text{E1})$$

where $\hbar\omega_{\mathbf{k}l}(t_{\text{pr}})$ is the l -th eigenvalue of $H'_{\mathbf{k}}(t_{\text{pr}})$, and

$$P_{\mathbf{k}ln}^{\text{qs}}(t_{\text{pr}}) = \sum_{n'} U_{\mathbf{k}n'l}^*(t_{\text{pr}}) P_{\mathbf{k}n'n}(t_{\text{pr}}). \quad (\text{E2})$$

Moreover, all of the coupling matrices \mathbf{J} , \mathbf{V} , \mathbf{D} and $\delta\mathbf{J}/\delta\mathbf{A}$ should be evaluated at the time t_{pr} and transformed using $U_{\mathbf{k}}(t_{\text{pr}})$. Performing some algebra, one obtains the two parts of quasi-static conductivity as,

$$\sigma_1^{\text{qs}}(\omega, t_{\text{pr}}) = \frac{ie^2}{\hbar\mathcal{V}} \sum_{\mathbf{k}} \sum_{l_1 l_2 l_3} \left\{ \begin{aligned} & -\frac{\mathbf{J}_{\mathbf{k}}^{l_2 l_1}(t_{\text{pr}}) \mathbf{V}_{\mathbf{k}}^{l_1 l_3}(t_{\text{pr}}) N_{\mathbf{k}l_2 l_3}(t_{\text{pr}})}{\omega_{\mathbf{k}l_1 l_3}(t_{\text{pr}}) [\omega_{\mathbf{k}l_2 l_3}(t_{\text{pr}}) + \omega + i0^+]} \\ & + \frac{\mathbf{J}_{\mathbf{k}}^{l_2 l_1}(t_{\text{pr}}) \mathbf{V}_{\mathbf{k}}^{l_1 l_3}(t_{\text{pr}}) N_{\mathbf{k}l_2 l_3}(t_{\text{pr}})}{\omega_{\mathbf{k}l_1 l_3}(t_{\text{pr}}) [\omega_{\mathbf{k}l_2 l_1}(t_{\text{pr}}) + \omega + i0^+]} \\ & + \frac{\mathbf{J}_{\mathbf{k}}^{l_3 l_2}(t_{\text{pr}}) \mathbf{V}_{\mathbf{k}}^{l_1 l_3}(t_{\text{pr}}) N_{\mathbf{k}l_1 l_2}(t_{\text{pr}})}{\omega_{\mathbf{k}l_1 l_3}(t_{\text{pr}}) [\omega_{\mathbf{k}l_1 l_2}(t_{\text{pr}}) + \omega + i0^+]} \\ & - \frac{\mathbf{J}_{\mathbf{k}}^{l_3 l_2}(t_{\text{pr}}) \mathbf{V}_{\mathbf{k}}^{l_1 l_3}(t_{\text{pr}}) N_{\mathbf{k}l_1 l_2}(t_{\text{pr}})}{\omega_{\mathbf{k}l_1 l_3}(t_{\text{pr}}) [\omega_{\mathbf{k}l_3 l_2}(t_{\text{pr}}) + \omega + i0^+]} \\ & + \frac{i\mathbf{J}_{\mathbf{k}}^{l_2 l_1}(t_{\text{pr}}) \mathbf{D}_{\mathbf{k}}^{l_1 l_3}(t_{\text{pr}}) N_{\mathbf{k}l_2 l_3}(t_{\text{pr}})}{\omega_{\mathbf{k}l_2 l_1}(t_{\text{pr}}) + \omega + i0^+} \\ & - \frac{i\mathbf{J}_{\mathbf{k}}^{l_3 l_2}(t_{\text{pr}}) \mathbf{D}_{\mathbf{k}}^{l_1 l_3}(t_{\text{pr}}) N_{\mathbf{k}l_1 l_2}(t_{\text{pr}})}{\omega_{\mathbf{k}l_3 l_2}(t_{\text{pr}}) + \omega + i0^+} \end{aligned} \right\}, \quad (\text{E3})$$

and

$$\sigma_2^{\text{qs}}(\omega, t_{\text{pr}}) = \frac{e}{\mathcal{V}} \sum_{\mathbf{k}} \sum_{l_1 l_2} \frac{iN_{\mathbf{k}l_1 l_2}(t_{\text{pr}}) \frac{\delta\mathbf{J}_{\mathbf{k}}^{l_1 l_2}(t_{\text{pr}})}{\delta\mathbf{A}}}{\omega_{\mathbf{k}l_1 l_2}(t_{\text{pr}}) + \omega + i0^+}, \quad (\text{E4})$$

where $\omega_{\mathbf{k}ll'}(t_{\text{pr}}) = \omega_{\mathbf{k}l}(t_{\text{pr}}) - \omega_{\mathbf{k}l'}(t_{\text{pr}})$ is the difference between eigenenergies of the time-dependent single-particle Hamiltonian at time t_{pr} , $N_{\mathbf{k}ll'}(t_{\text{pr}}) = \sum_n P_{\mathbf{k}ln}^{\text{qs}*}(t_{\text{pr}}) P_{\mathbf{k}l'n}^{\text{qs}}(t_{\text{pr}}) f_{\mathbf{k}n}$ is the dynamical population matrix of the corresponding eigenbasis, and in the derivation we have used the following property of the projection coefficients: $\sum_n P_{\mathbf{k}ln}^{\text{qs}*}(t_{\text{pr}}) P_{\mathbf{k}l'n}^{\text{qs}}(t_{\text{pr}}) = \delta_{ll'}$.

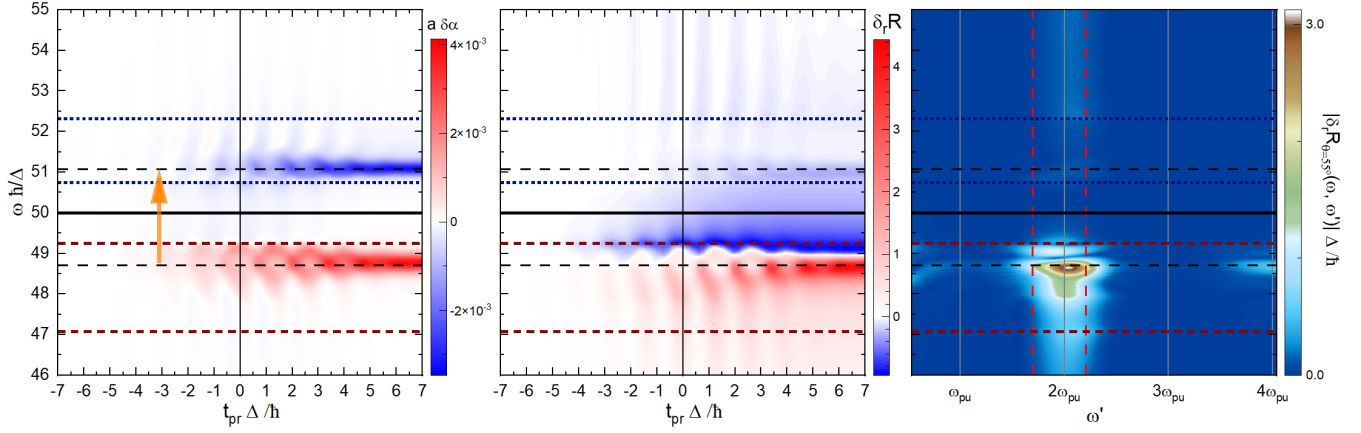


Figure 8. Transient optical behavior of the pumped system, computed using the quasi-static approximation. All parameters are similar to the ones of Fig. 2. (left) The transient differential absorption coefficient, (middle) the transient relative differential reflectivity at the incident angle of $\theta = 55^\circ$, and (right) the amplitude of the Fourier transformation of the transient reflectivity, $|\delta R_{\theta=55^\circ}(\omega, \omega')|$.

For the pumped toy-model with the parameters of Fig. 2 in the main text, we calculate the transient optical behavior, using quasi-static approximation and the results are shown in Fig. 8. Clearly, even though there are some similarities between the results presented in Figs. 8 and 2, many of the details of the full calculations are not captured in the quasi-static approximation.

Appendix F: A brief study on the damping factor (0^+)

As described in the main text (see Sec. IIF2), 0^+ should be chosen in such a way to make individual \mathbf{k} points on the grid indistinguishable. As such, for the case of the XUV probe, we chose it to be $0.05\Delta/\hbar$. In Fig. 9 top panel, we plot the equilibrium dielectric function in the XUV regime, with $0^+ = 0.02\Delta/\hbar$ and compare it with the case of $0^+ = 0.05\Delta/\hbar$, which is used in all of the XUV calculations in the main text. Clearly, the small value of $0^+ = 0.02\Delta/\hbar$ introduces fluctuations which are the distinguishable effects of individual \mathbf{k} points on the grid. The inset magnifies the low values of the y axis and shows how the smaller 0^+ makes $\text{Im}[\epsilon^{\text{eq}}(\omega)]$ vanish more rapidly outside of the energy range of the CB. This confirms our explanation that the broadening of $\text{Im}[\epsilon^{\text{eq}}(\omega)]$ outside of the energy range of the CB is because of the finite value of 0^+ .

Going to the IR-V regime, we work with lower frequencies which makes the results more sensitive to the energy differences between adjacent \mathbf{k} points on the grid and calls for a larger damping factor. In Fig. 9 bottom panel, we plot the equilibrium dielectric function in the IR-V regime, with $0^+ = 0.05\Delta/\hbar$ and compare it with the case of $0^+ = 0.1\Delta/\hbar$, which is used in the IR-V calculations in the main text. Clearly, even though the value $0^+ = 0.05\Delta/\hbar$ works well for the XUV regime, for

the IR-V regime it is not adequate. On the other hand, using the more reliable value of $0^+ = 0.1\Delta/\hbar$ has the problem that for the low frequencies outside of the gap-energy range, $\text{Im}[\epsilon^{\text{eq}}(\omega)]$ doesn't vanish rapidly enough, and there is no way out of such limitations.

Appendix G: Transient differential dielectric function

In this appendix, we show the transient differential imaginary and real parts of the dielectric function, i.e.,

$$\delta \text{Im} \epsilon(\omega, t_{\text{pr}}) = \text{Im}[\epsilon(\omega, t_{\text{pr}}) - \epsilon^{\text{eq}}(\omega)], \quad (\text{G1})$$

and

$$\delta \text{Re} \epsilon(\omega, t_{\text{pr}}) = \text{Re}[\epsilon(\omega, t_{\text{pr}}) - \epsilon^{\text{eq}}(\omega)], \quad (\text{G2})$$

respectively, where $\epsilon^{\text{eq}}(\omega) = \epsilon(\omega, t_{\text{pr}} \rightarrow t_{\text{ini}})$ is the equilibrium dielectric function.

Fig. 10 shows the transient behavior of the differential imaginary and real parts of the dielectric function, with the same parameters as the ones of Fig. 2. Comparison between Figs. 2 and 10, one can see that the behavior of the absorption coefficient can be qualitatively very well understood by studying just $\text{Im} \epsilon(\omega, t_{\text{pr}})$, as it is also clear from the Eq. 45. Moreover, the transient reflectivity behavior can also be qualitatively understood to some extent from the transient real part of the dielectric function, $\text{Re} \epsilon(\omega, t_{\text{pr}})$, as the latter is the main ingredient of the refractive index and hence plays a major role in determining the former.

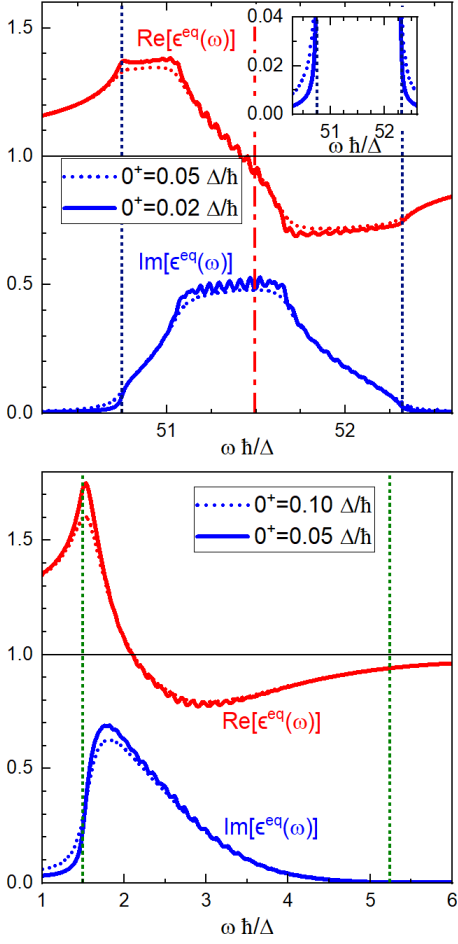


Figure 9. (top) The equilibrium dielectric function in the XUV regime. The solid curves correspond to $0^+ = 0.02\Delta/\hbar$, while the dotted curves correspond to $0^+ = 0.05\Delta/\hbar$, which is used in the XUV calculations in the main text. The inset magnifies the low values of the y axis and shows how the smaller 0^+ makes $\text{Im}[\epsilon^{\text{eq}}(\omega)]$ vanish more rapidly outside of the energy range of the CB. (bottom) The equilibrium dielectric function in the IR-V regime. The solid curves correspond to $0^+ = 0.05\Delta/\hbar$, while the dotted curves correspond to $0^+ = 0.1\Delta/\hbar$, as used in Fig. 7.

Appendix H: Density of states and its generalizations

We define the density of states, $g(\varepsilon)$, at each energy ε as the number of states within the infinitesimal range $d\varepsilon$ around ε divided by $d\varepsilon$, in the volume of the unit cell. Even though mathematically, $g(\varepsilon)$ is defined using a Dirac-delta function, in numerical calculations it is obtained as,

$$g(\varepsilon) = \frac{1}{N_{\text{grid}}} \sum_{\mathbf{k} \in \text{grid}} \sum_n L(\varepsilon - \varepsilon_{\mathbf{k},n}), \quad (\text{H1})$$

where $L(\varepsilon) = \frac{\hbar 0^+}{\pi(\hbar^2 0^{+2} + \varepsilon^2)}$ is the Lorentzian function. This concept can be generalized to any momentum and

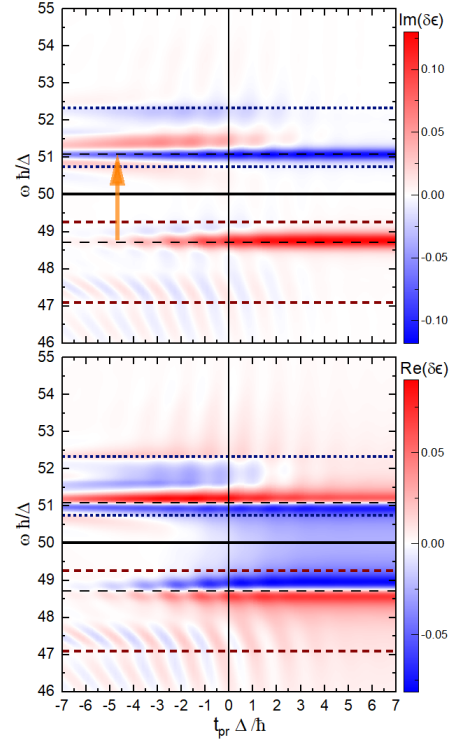


Figure 10. Transient behavior of the differential (left) imaginary part of the dielectric function, $\delta \text{Im} \epsilon(\omega, t_{\text{pr}})$, and (right) its real part, $\delta \text{Re} \epsilon(\omega, t_{\text{pr}})$, vs the probe time and photon energy, with the same parameters as the ones of Fig. 2.

band dependent property, $O_{\mathbf{k},n}$, such as diagonal velocity and inverse-mass, etc., with the density given by:

$$g_{\mathcal{O}}(\varepsilon) = \frac{1}{N_{\text{grid}}} \sum_{\mathbf{k} \in \text{grid}} \sum_n O_{\mathbf{k},n} L(\varepsilon - \varepsilon_{\mathbf{k},n}). \quad (\text{H2})$$

Another generalization is to compute the n_{ph} -photon density of resonant states (DORS). Roughly speaking, the n_{ph} transitions come from the n_{ph} -th power of the pumping field. We define the function $w_{n_{\text{ph}}}(\varepsilon_{\text{gap}})$ which gives the strength of the n_{ph} resonance for each given gap-energy ε_{gap} , and is obtained from the leading term of the square of the amplitude of the $\varepsilon_{\text{gap}}/\hbar$ component in the spectrum of the n_{ph} -th power of the pump pulse, centered at $n_{\text{ph}}\omega_{\text{pu}}$. With our pump, Eq. 69, it is given by [49]

$$w_{n_{\text{ph}}}(\varepsilon_{\text{gap}}) = e^{-\frac{\tau_{\text{pu}}^2}{8n_{\text{ph}} \ln 2} \left(\frac{\varepsilon_{\text{gap}}}{\hbar} - n_{\text{ph}}\omega_{\text{pu}}\right)^2}. \quad (\text{H3})$$

This strength function is normalized so that at the exact resonance, $\varepsilon_{\text{gap}} = \hbar n_{\text{ph}}\omega_{\text{pu}}$, it is equal to 1. Note that, instead of the amplitude, its square is used, as in a pure Rabi-oscillation with low Rabi frequency, the excitation population is proportional to the square of the pump amplitude [49]. Nevertheless, one should be aware of the fact that different frequency components of the pump pulse do

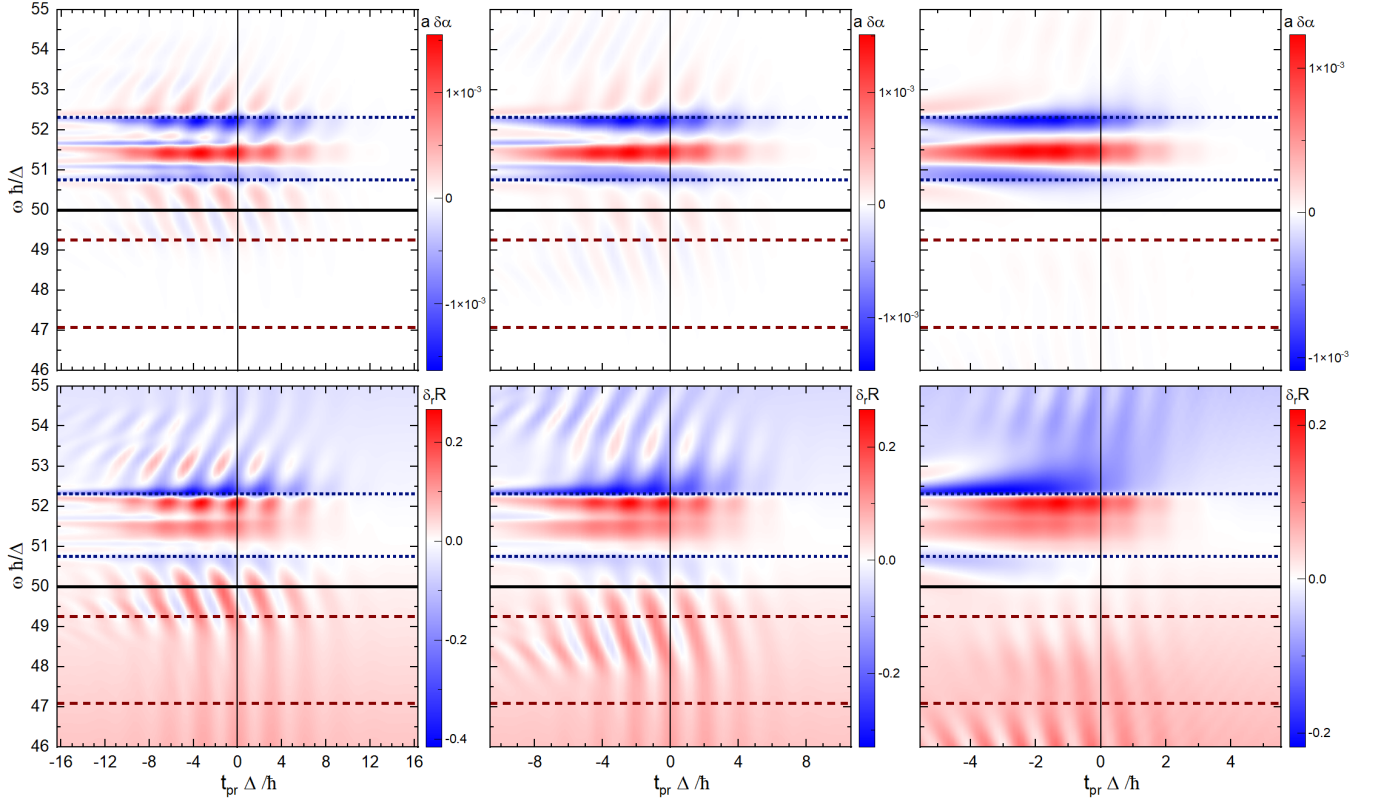


Figure 11. Only intra-band transitions in the dynamics. (top row) Transient differential absorption coefficients and (bottom row) transient relative differential reflectivities for three different pump-pulse frequencies: (left column) $\hbar\omega_{\text{pu}}/\Delta = 1$, (middle column) $\hbar\omega_{\text{pu}}/\Delta = 1.5$ and (right column) $\hbar\omega_{\text{pu}}/\Delta = 3$, and the rest of the parameter are similar to the corresponding panels of Fig. 5.

not act independently, and hence our resonance assignment should be considered as an approximation. Usually, the gaps between the filled and empty bands are of interest. At zero temperature, the n_{ph} -photon DORS is given by

$$g_{n_{\text{ph}}}(\varepsilon) = \frac{1}{N_{\text{grid}}} \sum_{\mathbf{k} \in \text{grid}} \sum_{n_C} L(\varepsilon - \varepsilon_{\mathbf{k}, n_C}) \sum_{n_V} w_{n_{\text{ph}}}(\varepsilon_{\mathbf{k}, n_C} - \varepsilon_{\mathbf{k}, n_V}), \quad \varepsilon > \varepsilon_F \quad (\text{H4})$$

$$g_{n_{\text{ph}}}(\varepsilon) = \frac{1}{N_{\text{grid}}} \sum_{\mathbf{k} \in \text{grid}} \sum_{n_V} L(\varepsilon - \varepsilon_{\mathbf{k}, n_V}) \sum_{n_C} w_{n_{\text{ph}}}(\varepsilon_{\mathbf{k}, n_C} - \varepsilon_{\mathbf{k}, n_V}), \quad \varepsilon < \varepsilon_F \quad (\text{H5})$$

where n_C (n_V) runs over the CBs (VBs) and ε_F is the Fermi energy. For finite temperatures, we consider the gaps between the filled and empty electronic states, and consequently, generalize $g_{n_{\text{ph}}}(\varepsilon)$ by obtaining it as,

$$g_{n_{\text{ph}}}(\varepsilon) = \frac{1}{N_{\text{grid}}} \sum_{\mathbf{k} \in \text{grid}} \sum_{nn'} [f_{\mathbf{k}, n}(1 - f_{\mathbf{k}, n'}) + f_{\mathbf{k}, n'}(1 - f_{\mathbf{k}, n})] L(\varepsilon - \varepsilon_{\mathbf{k}, n}) w_{n_{\text{ph}}}(|\varepsilon_{\mathbf{k}, n} - \varepsilon_{\mathbf{k}, n'}|). \quad (\text{H6})$$

Appendix I: Intra-band motion with different pump-pulse frequencies

In Fig. 11, we show the transient differential absorption coefficient and relative differential reflectivity with considering only intra-band transitions upon pumping, for three different pump frequencies, $\hbar\omega_{\text{pu}}/\Delta = 1, 1.5, 3$, similar to Fig. 5. Clearly, the color maps are qualitatively very similar, i.e., the probe photon energies at which positive or negative (red or blue, respectively) features appear, are almost independent of the frequency of the pump pulse, even though the details of the oscillations vary by varying it.

-
- [1] T. Brabec and F. Krausz, *Reviews of Modern Physics* **72**, 545 (2000).
- [2] F. Krausz and M. Ivanov, *Reviews of modern physics* **81**, 163 (2009).
- [3] F. Krausz and M. I. Stockman, *Nature Photonics* **8**, 205 (2014).
- [4] F. Calegari, G. Sansone, S. Stagira, C. Vozzi, and M. Nisoli, *Journal of Physics B: Atomic, Molecular and Optical Physics* **49**, 062001 (2016).
- [5] R. Borrego-Varillas, M. Lucchini, and M. Nisoli, *Reports on Progress in Physics* **85**, 066401 (2022).
- [6] M. Zürich, H.-T. Chang, L. J. Borja, P. M. Kraus, S. K. Cushing, A. Gandman, C. J. Kaplan, M. H. Oh, J. S. Prell, D. Prendergast, C. D. Pemmaraju, D. M. Neumark, and S. R. Leone, *Nature Communications* **8**, 15734 (2017).
- [7] M. Zürich, H.-T. Chang, P. M. Kraus, S. K. Cushing, L. J. Borja, A. Gandman, C. J. Kaplan, M. H. Oh, J. S. Prell, D. Prendergast, C. D. Pemmaraju, D. M. Neumark, and S. R. Leone, *Structural Dynamics* **4**, 044029 (2017).
- [8] C. J. Kaplan, P. M. Kraus, A. D. Ross, M. Zürich, S. K. Cushing, M. F. Jager, H.-T. Chang, E. M. Gullikson, D. M. Neumark, and S. R. Leone, *Phys. Rev. B* **97**, 205202 (2018).
- [9] L. Perfetti, P. A. Loukakos, M. Lisowski, U. Bovensiepen, M. Wolf, H. Berger, S. Biermann, and A. Georges, *New Journal of Physics* **10**, 053019 (2008).
- [10] F. Schmitt, P. S. Kirchmann, U. Bovensiepen, R. G. Moore, L. Rettig, M. Krenz, J.-H. Chu, N. Ru, L. Perfetti, D. Lu, *et al.*, *Science* **321**, 1649 (2008).
- [11] D. von der Linde, T. Engers, G. Jenke, P. Agostini, G. Grillon, E. Nibbering, A. Mysyrowicz, and A. Antonetti, *Physical Review A* **52**, R25 (1995).
- [12] P. A. Norreys, M. Zepf, S. Moustazis, A. P. Fews, J. Zhang, P. Lee, M. Bakarezos, C. N. Danson, A. Dyson, P. Gibbon, P. Loukakos, D. Neely, F. N. Walsh, J. S. Wark, and A. E. Dangor, *Phys. Rev. Lett.* **76**, 1832 (1996).
- [13] A. H. Chin, O. G. Calderón, and J. Kono, *Physical Review Letters* **86**, 3292 (2001).
- [14] S. Ghimire, A. D. DiChiara, E. Sistrunk, P. Agostini, L. F. DiMauro, and D. A. Reis, *Nature physics* **7**, 138 (2011).
- [15] T. T. Luu, M. Garg, S. Y. Kruchinin, A. Moulet, M. T. Hassan, and E. Goulielmakis, *Nature* **521**, 498 (2015).
- [16] S. Han, H. Kim, Y. W. Kim, Y.-J. Kim, S. Kim, I.-Y. Park, and S.-W. Kim, *Nature communications* **7**, 13105 (2016).
- [17] L. J. Borja, M. Zürich, C. D. Pemmaraju, M. Schultze, K. Ramasesha, A. Gandman, J. S. Prell, D. Prendergast, D. M. Neumark, and S. R. Leone, *J. Opt. Soc. Am. B* **33**, C57 (2016).
- [18] Y. S. You, D. A. Reis, and S. Ghimire, *Nature physics* **13**, 345 (2017).
- [19] H. Liu, Y. Li, Y. S. You, S. Ghimire, T. F. Heinz, and D. A. Reis, *Nature Physics* **13**, 262 (2017).
- [20] S. Jiang, S. Gholam-Mirzaei, E. Crites, J. E. Beetar, M. Singh, R. Lu, M. Chini, and C. Lin, *Journal of Physics B: Atomic, Molecular and Optical Physics* **52**, 225601 (2019).
- [21] T. Rohwer, S. Hellmann, M. Wiesenmayer, C. Sohr, A. Stange, B. Slomski, A. Carr, Y. Liu, L. M. Avila, M. Källäne, *et al.*, *Nature* **471**, 490 (2011).
- [22] C. L. Smallwood, J. P. Hinton, C. Jozwiak, W. Zhang, J. D. Koralek, H. Eisaki, D.-H. Lee, J. Orenstein, and A. Lanzara, *Science* **336**, 1137 (2012).
- [23] S. Hellmann, T. Rohwer, M. Källäne, K. Hanff, C. Sohr, A. Stange, A. Carr, M. Murnane, H. Kapteyn, L. Kipp, *et al.*, *Nature communications* **3**, 1069 (2012).
- [24] E. Papalazarou, J. Faure, J. Mauchain, M. Marsi, A. Taleb-Ibrahimi, I. Reshetnyak, A. van Rookeghem, I. Timrov, N. Vast, B. Arnaud, and L. Perfetti, *Phys. Rev. Lett.* **108**, 256808 (2012).
- [25] Y. Wang, H. Steinberg, P. Jarillo-Herrero, and N. Gedik, *Science* **342**, 453 (2013).
- [26] J. C. Johannsen, S. Ulstrup, F. Cilento, A. Crepaldi, M. Zacchigna, C. Cacho, I. C. E. Turcu, E. Springate, F. Fromm, C. Roidel, T. Seyller, F. Parmigiani, M. Grioni, and P. Hofmann, *Phys. Rev. Lett.* **111**, 027403 (2013).
- [27] J. Rameau, S. Freutel, A. Kemper, M. A. Sentef, J. Freericks, I. Avigo, M. Ligges, L. Rettig, Y. Yoshida, H. Eisaki, *et al.*, *Nature communications* **7**, 13761 (2016).
- [28] J. Reimann, S. Schlauderer, C. Schmid, F. Langer, S. Baierl, K. Kokh, O. Tereshchenko, A. Kimura, C. Lange, J. Güdde, *et al.*, *Nature* **562**, 396 (2018).
- [29] M. Schultze, E. M. Bothschafter, A. Sommer, S. Holzner, W. Schweinberger, M. Fiess, M. Hofstetter, R. Kienberger, V. Apalkov, V. S. Yakovlev, *et al.*, *Nature* **493**, 75 (2013).
- [30] L. Stojchevska, I. Vaskivskiy, T. Mertelj, P. Kusar, D. Svetin, S. Brazovskii, and D. Mihailovic, *Science* **344**, 177 (2014).
- [31] M. Schultze, K. Ramasesha, C. Pemmaraju, S. Sato, D. Whitmore, A. Gandman, J. S. Prell, L. Borja, D. Prendergast, K. Yabana, *et al.*, *Science* **346**, 1348 (2014).
- [32] M. Lucchini, S. A. Sato, A. Ludwig, J. Herrmann, M. Volkov, L. Kasmi, Y. Shinohara, K. Yabana, L. Gallmann, and U. Keller, *Science* **353**, 916 (2016).
- [33] H. Mashiko, K. Oguri, T. Yamaguchi, A. Suda, and H. Gotoh, *Nature physics* **12**, 741 (2016).
- [34] M. Zürich, H.-T. Chang, P. M. Kraus, S. K. Cushing, L. J. Borja, A. Gandman, C. J. Kaplan, M. H. Oh, J. S. Prell, D. Prendergast, *et al.*, *Structural Dynamics* **4**, 044029 (2017).
- [35] F. Schlaepfer, M. Lucchini, S. A. Sato, M. Volkov, L. Kasmi, N. Hartmann, A. Rubio, L. Gallmann, and U. Keller, *Nature Physics* **14**, 560 (2018).
- [36] C. J. Kaplan, P. M. Kraus, E. M. Gullikson, L. J. Borja, S. K. Cushing, M. Zürich, H.-T. Chang, D. M. Neumark, and S. R. Leone, *J. Opt. Soc. Am. B* **36**, 1716 (2019).
- [37] R. Geneaux, H. J. Marroux, A. Guggenmos, D. M. Neumark, and S. R. Leone, *Philosophical Transactions of the Royal Society A* **377**, 20170463 (2019).
- [38] G. Inzani, L. Adamska, A. Eskandari-asl, N. D. Palo, G. L. Dolso, B. Moio, L. J. D'Onofrio, A. Lamperti, A. Molle, R. Borrego-Varillas, M. Nisoli, S. Pittalis, C. A. Rozzi, A. Avella, and M. Lucchini, *Nature Photonics* , 1 (2023).

- [39] G. Inzani, A. Eskandari-asl, L. Adamska, B. Moio, G. L. Dolso, N. D. Palo, L. J. D’Onofrio, A. Lamperti, A. Molle, C. A. Rozzi, R. Borrego-Varillas, M. Nisoli, S. Pittalis, A. Avella, and M. Lucchini, *IL NUOVO CIMENTO C* **46**, 1 (2023).
- [40] U. De Giovannini, G. Brunetto, A. Castro, J. Walkenhorst, and A. Rubio, *ChemPhysChem* **14**, 1298 (2013).
- [41] U. De Giovannini, H. Hubener, and A. Rubio, *Nano letters* **16**, 7993 (2016).
- [42] P. Wopperer, U. De Giovannini, and A. Rubio, *The European Physical Journal B* **90**, 1 (2017).
- [43] U. De Giovannini, H. Hübener, and A. Rubio, *Journal of chemical theory and computation* **13**, 265 (2017).
- [44] C. D. Pemmaraju, F. D. Vila, J. J. Kas, S. A. Sato, J. J. Rehr, K. Yabana, and D. Prendergast, *Computer Physics Communications* **226**, 30 (2018).
- [45] N. Tancogne-Dejean and A. Rubio, *Science advances* **4**, eaao5207 (2018).
- [46] U. De Giovannini, A. Castro, *et al.*, *Attosecond Molecular Dynamics* **13**, 424 (2018).
- [47] O. Neufeld, N. Tancogne-Dejean, U. De Giovannini, H. Hübener, and A. Rubio, *npj Computational Materials* **9**, 39 (2023).
- [48] G. S. Armstrong, M. A. Khokhlova, M. Labeye, A. S. Maxwell, E. Pisanty, and M. Ruberti, *The European Physical Journal D* **75**, 209 (2021).
- [49] A. Eskandari-asl and A. Avella, *arXiv preprint arXiv:2307.01244* (2023).
- [50] M. Schüler, J. A. Marks, Y. Murakami, C. Jia, and T. P. Devereaux, *Physical Review B* **103**, 155409 (2021).
- [51] J. R. Yates, X. Wang, D. Vanderbilt, and I. Souza, *Phys. Rev. B* **75**, 195121 (2007).